

Clara Orbe^{1,2}, David Rind¹, Ron L Miller¹, Larissa S Nazarenko^{1,3}, Anastasia Romanou^{1,2}, Jeffrey Jonas^{1,3}, Gary L Russell¹, Maxwell Kelley¹, and Gavin A Schmidt¹

¹NASA Goddard Institute for Space Studies

²Department of Applied Physics and Applied Mathematics, Columbia University

³Center for Climate Systems Research, Earth Institute, Columbia University

May 31, 2023

**Atmospheric Response to a Collapse of the North Atlantic Circulation Under
A Mid-Range Future Climate Scenario: A Regime Shift in Northern
Hemisphere Dynamics**

Clara Orbe^{a,b}, David Rind^a, Ron L. Miller^a, Larissa S. Nazarenko^{a,c}, Anastasia Romanou^{a,b},
Jeffrey Jonas^{a,c}, Gary L. Russell^a, Maxwell Kelley^a, and Gavin A. Schmidt^a

^a *NASA Goddard Institute for Space Studies, New York, NY*

^b *Department of Applied Physics and Applied Mathematics, Columbia University, New York, NY*

^c *Center for Climate Systems Research, Earth Institute, Columbia University, New York, NY*

Corresponding author: Clara Orbe, clara.orbe@nasa.gov

10 ABSTRACT: Climate models project a future weakening of the Atlantic Meridional Overturning
11 Circulation (AMOC), but the impacts of this weakening on climate remain highly uncertain. A
12 key challenge in quantifying the impact of an AMOC decline is in isolating its influence on
13 climate, relative to other changes associated with increased greenhouse gases. Here we isolate
14 the climate impacts of a weakened AMOC in the broader context of a warming climate using a
15 unique ensemble of Shared Socioeconomic Pathway (SSP) 2-4.5 integrations that was performed
16 using the Climate Model Intercomparison Project Phase 6 (CMIP6) version of the NASA Goddard
17 Institute for Space Studies ModelE (E2.1). In these runs internal variability alone results in a
18 spontaneous bifurcation of the ocean flow, wherein two out of ten ensemble members exhibit an
19 entire AMOC collapse, while the other eight recover at various stages despite identical forcing
20 of each ensemble member and with no externally prescribed freshwater perturbation. We show
21 that an AMOC collapse results in an abrupt northward shift and strengthening of the Northern
22 Hemisphere (NH) HC and intensification of the northern midlatitude eddy-driven jet. We then
23 use a set of coupled atmosphere-ocean abrupt CO₂ experiments spanning the range 1-5xCO₂ to
24 show that this response to an AMOC collapse results in a nonlinear shift in the NH circulation
25 moving from 2xCO₂ to 3xCO₂. Slab-ocean versions of these experiments, by comparison, do not
26 capture this nonlinear behavior. Our results suggest that changes in ocean heat flux convergences
27 associated with an AMOC collapse — while highly uncertain — can result in profound changes in
28 the NH circulation and continued efforts to constrain the AMOC response to future climate change
29 are needed.

30 1. Introduction

31 Future projections of the atmospheric circulation remain highly uncertain and reflect uncertainties
32 in the direct radiative response to CO₂ forcing (Deser and Phillips (2009); Grise and Polvani (2014);
33 Shaw and Voigt (2015); Ceppi et al. (2018)), as well as both the (direct) response to changes in sea
34 surface temperatures (SSTs) and the (indirect) response to changes in eddy feedbacks (see Shepherd
35 (2014) and references therein). Uncertainties in SST projections over the subpolar North Atlantic
36 are particularly consequential, as they strongly influence the location and strength of the North
37 Atlantic storm track, with profound downstream impacts on precipitation and wintertime weather
38 over Europe and parts of Africa (e.g., Zhang and Delworth (2006), Smith et al. (2010), Woollings
39 et al. (2012), O'Reilly et al. (2016)). In particular, while increases in greenhouse gases over the
40 21st century are expected to result in substantial warming over much of the North Atlantic, climate
41 models project considerable cooling over midlatitudes resulting in a so-called “North Atlantic
42 warming hole (NAWH)” (e.g., Josey et al. (2018), Drijfhout et al. (2012), Robson et al. (2016),
43 Caesar et al. (2018)). While the drivers of this NAWH have been under considerable debate, recent
44 detection-attribution analysis suggests that the anthropogenic signal of the NAWH has emerged
45 from internal climate variability and, moreover, that this cooling can be attributed to declining
46 northward oceanic heat flux over recent decades related to increased greenhouse gas emissions
47 (Chemke et al. (2022)).

48 Among other mechanisms contributing to the development of the NAWH, the slowdown of
49 the Atlantic Meridional Overturning Circulation (AMOC) has been invoked as one potential key
50 driver (Cheng et al. (2013), Rahmstorf et al. (2015), Menary and Wood (2018)). Studies have
51 long shown that changes in the strength of the AMOC can have widespread impacts not only
52 on other components of the ocean circulation but, more generally, on the broader atmospheric
53 climate system, resulting in a southward shift of the intertropical convergence zone (ITCZ) (e.g.,
54 Zhang and Delworth (2005), Vellinga and Wood (2008), Jackson et al. (2015)), a strengthening
55 of the Walker circulation (e.g., Vial et al. (2018), Orihuela-Pinto et al. (2022)) and a northward
56 shift of the Northern Hemisphere (NH) jet stream (e.g., Liu et al. (2020), Bellomo et al. (2021)).
57 Understanding the global scale atmospheric response to changes in AMOC strength is important
58 not only for projections of future climate, but also for understanding paleoclimate records and
59 the dynamics of past Dansgaard-Oeschger events. In particular, while the future collapse of an

60 AMOC is still considered unlikely, the latest generation of coupled climate models project stronger
61 weakening with future warming, compared to older generations of models (Weijer et al. (2020)).

62 In addition to its impacts on global precipitation, SST-related changes in the AMOC can change
63 the baroclinicity of the atmosphere, which can result in changes in the storm tracks (Woollings
64 et al. (2012)). However, the precise impacts of a weakened AMOC on atmospheric baroclinity
65 are not well understood, largely because studies have used models that exhibit a wide diversity
66 in the amplitude and spatial extent of the NAWH (Gervais et al. (2019), Haarsma et al. (2015),
67 Menary and Wood (2018)). Nonetheless, despite these uncertainties in the drivers and extent of
68 the NAWH, Woollings et al. (2012) showed that the response of the North Atlantic storm track to
69 climate change was singularly shaped by changes in ocean-atmosphere coupling.

70 The role of the AMOC in future projections of the jet stream in the Climate Model Intercom-
71 parison Project Phase 5 (CMIP5) and Phase 6 (CMIP6) models was recently examined in Bellomo
72 et al. (2021) (hereafter KB2021), who showed that changes in the AMOC play a primary role
73 in determining the magnitude of the projected poleward displacement of the NH zonal mean jet
74 stream. In particular, by stratifying models according to the strength of their projected AMOC
75 weakening (in response to a quadrupling of CO₂), the authors showed that models with a larger
76 AMOC decline (> 7 Sv, relative to preindustrial values) exhibit minimum warming over the North
77 Atlantic, a southward displacement of the ITCZ and a poleward shift of the northern midlatitude
78 jet. The results from KB2021 suggest that the AMOC is a major driver of intermodal uncertainty
79 in future projections of the northern jet stream (and associated hydrological impacts).

80 A key challenge in quantifying the impact of AMOC uncertainties on future projections of the
81 large-scale atmospheric circulation is in isolating its influence on climate, relative to other changes
82 associated with increased greenhouse gases. Thus, while the results from KB2021 are compelling,
83 that study drew conclusions based on the spread among models subject to the same abrupt 4xCO₂
84 forcing and it is not clear if the models exhibiting greater AMOC weakening were also models
85 that exhibit other characteristics that would independently impact the jet stream. At the same time,
86 previous studies using more traditional freshwater flux perturbations to examine the jet (and other
87 climate) responses to a weakened AMOC, have done so in the absence of other background changes
88 related to increased CO₂ (e.g., Zhang and Delworth (2005), Jackson et al. (2015)). As such, these

89 studies may produce a circulation response to a weakened AMOC that is different than what might
90 occur if other factors impacting atmospheric temperature gradients are included.

91 One recent attempt to isolate the climate impacts of a weakened AMOC in the broader context
92 of a warming climate was performed in Liu et al. (2020). In that study, the authors compared fully
93 coupled Representative Concentration Pathway (RCP) 8.5 simulations (Riahi et al. (2011)) using a
94 full physics comprehensive model (CCSM4) with identically forced simulations in which a negative
95 freshwater perturbation over the subpolar North Atlantic was added after year 1980 in order to
96 maintain the AMOC strength (while preserving all other forcings). That study showed results
97 that were generally consistent with KB2021, pointing to a major role of the AMOC in causing
98 widespread cooling stretching from NH high latitudes to the tropics and a poleward displacement
99 of the NH midlatitude jet.

100 While the results from Liu et al. (2020) represent an important step forward in isolating the
101 impacts of the AMOC on the storm tracks in the context of a warming climate, it is not clear
102 that prescribing a negative freshwater perturbation does not potentially interfere with nonlinear
103 components of the AMOC response in a coupled system. To this end, here we present new results
104 featuring an ensemble of Shared Socioeconomic Pathway (SSP) 2-4.5 integrations (Meinshausen
105 et al. (2020)) that was performed using the CMIP6 version of the NASA Goddard Institute for
106 Space Studies (GISS) ModelE (E2.1) (Kelley et al. (2020)). In particular, we show results from a
107 subset of the runs documented in Romanou et al. (2023) (hereafter AR2023), in which the authors
108 identified a tipping point in the SSP 2-4.5 ensemble occurring during the “extended” portion of
109 the simulations (i.e. beyond year 2090, after which CO₂ emissions are ramped down). During this
110 time period the authors show that internal variability alone results in a spontaneous bifurcation of
111 the ocean flow, wherein two out of ten ensemble members exhibit an entire AMOC collapse, while
112 the other eight recover at various stages (Figure 1a). Note that, in contrast to the aforementioned
113 freshwater hosing studies, in which an AMOC collapse is induced by adding freshwater, in these
114 experiments the AMOC collapse is caused by a reduction in evaporation from the ocean, mediated
115 by sea ice melting (AR2023). As such, the atmospheric configuration that is used to produce this
116 effect in an interactive mode is likely to be very different from an atmosphere which is simply
117 responding to a prescribed freshwater flux perturbation.

118 Whereas AR2023 focused primarily on the oceanic conditions giving rise to this divergence in
119 AMOC behavior among different ensemble members, here we focus on the subsequent impacts
120 this has on the atmospheric large-scale circulation. In particular, we contrast the behavior between
121 two and eight ensemble members in which the AMOC respectively collapses and recovers to
122 historical values by year 2400 (red vs. green lines, Fig. 1a). As such, we isolate the impact of
123 a weakened AMOC on the atmospheric circulation in the presence of increased greenhouse gas
124 warming using a single model (unlike KB2021) and without any need to invoke negative freshwater
125 perturbations (as in Liu et al. (2020)). To the best of our knowledge, this represents the first time
126 that the AMOC imprint on the circulation has been isolated in the context of background increases
127 in greenhouse gases using a fully coupled comprehensive model, absent any externally imposed
128 freshwater perturbations that may potentially interfere with the model's internal dynamics.

129 As discussed in AR2023, the ensemble members in which the AMOC collapses are substantially
130 cooler than those runs in which it recovers, with wintertime global mean surface temperature
131 (GMST) differences of about 1°C by year 2400 (Fig. 1c). Therefore, in documenting the influence
132 of the AMOC on the atmosphere in the different SSP 2-4.5 ensemble members it is natural to ask how
133 the large-scale thermodynamic and dynamical circulations scale with these differences in GMST.
134 Though perhaps naive, it is common practice to assume that the climate system scales linearly with
135 GMST, as reflected in the use of so-called “global warming levels” in the recent IPCC AR6 report
136 (James et al. (2017)) and the widely applied related practice of “pattern scaling” (e.g., Santer et al.
137 (1990), Tebaldi and Arblaster (2014)). Recent studies, however, have shown that the climate's
138 so-called “dynamical sensitivity” – in particular, circulation shifts associated with changes in the
139 Hadley Cell and storm tracks - do not simply scale with equilibrium climate sensitivity across the
140 CMIP5 models (Grise and Polvani (2016)) and strongly depend on the evolution of SST warming
141 patterns in individual climate models (Ceppi et al. (2018)). As those studies, however, focused on
142 large (CMIP5) multi-model ensembles, it is not clear if similar conclusions also apply to single
143 models and to climate states in which the AMOC has undergone a substantial weakening. More
144 precisely, it remains unclear how much of the circulation response to a weakened AMOC is related
145 simply to changes in GMST or, rather, to changes in (free-tropospheric) meridional temperature
146 gradients away from the surface.

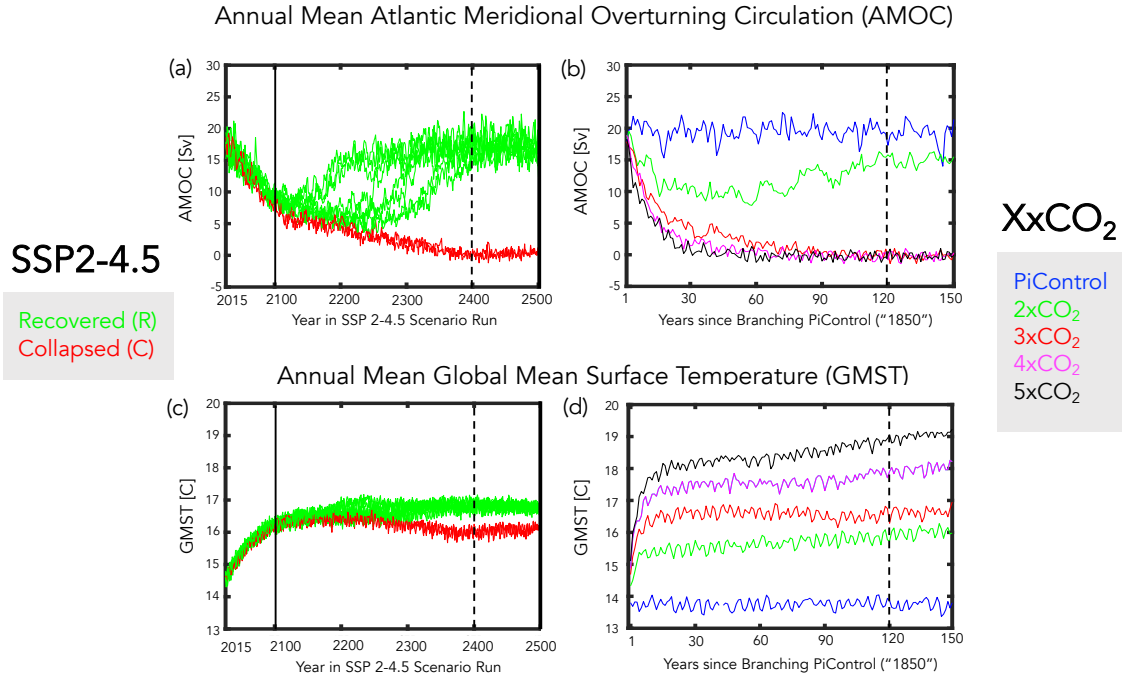


FIG. 1. Top: Evolution of the annual mean maximum overturning streamfunction in the Atlantic ocean, evaluated at 48°N, compared among the SSP 2-4.5 (8) recovered and (2) collapsed ensemble members (top, left) and among the abrupt XxCO₂ runs (top, right). Bottom: Same as top panels, except showing annual mean global surface temperature (GMST). Vertical solid lines mark the beginning of the “extension” portion of the SSP 2-4.5 scenario. Vertical dashed lines indicate the years after which climatological averages are evaluated (i.e., years 2400-2500 (left) and years 120-150 (right)).

To this end, in addition to reporting on the results from the SSP 2-4.5 ensemble we also examine a suite of abrupt 1-5xCO₂ experiments that were conducted using the same model version (Mitevski et al. (2021)). In particular, we exploit the fact that between 2xCO₂ and 3xCO₂ abrupt forcing the AMOC respectively recovers and collapses by year 150 (Fig. 1b), behavior which is generally similar to the differences in AMOC responses between the recovered and collapsed members of the SSP 2-4.5 ensemble, hereafter referred to as SSP 2-4.5 R and SSP 2-4.5 C, respectively (Fig. 1a). However, by spanning a much broader range of GMST changes, compared to the SSP 2-4.5 ensemble – and assuming that the atmospheric responses to an AMOC collapse are similar between the 3xCO₂ and SSP 2-4.5 collapsed ensemble members (a point which we examine in Section 3a3) – the broader set of XxCO₂ experiments affords a unique opportunity to investigate the relationship between dynamical sensitivity and GMST changes in the presence of a collapsed AMOC.

164 In Section 3 we begin by contrasting the large-scale atmospheric circulation responses between
165 the SSP 2-4.5 R and C members in which the AMOC recovers and remains collapsed after year
166 2400 (Sections 3a1-2, Q1 below). We then compare this behavior with the circulation differences
167 occurring in the 2xCO₂ and 3xCO₂ integrations (Section 3a3, Q2). After showing that the 3xCO₂
168 circulation changes in the NH are largely dominated by the behavior of the AMOC, we then use the
169 broader set of 1-5xCO₂ abrupt experiments to examine how the collapse of the AMOC modulates
170 the relationship between the NH dynamical circulation and GMST over a much broader range of
171 CO₂ forcing (Section 3b, Q3). In addressing the latter we also use slab-ocean model integrations
172 in order to examine if the behavior exhibited in the coupled atmosphere-ocean runs is reflected in
173 simulations in which ocean heat flux convergence changes associated with an AMOC collapse are
174 not allowed to occur. Finally, to interpret the CO₂ scaling results we examine the compensation
175 that arises between the ocean and atmosphere in response to a decline and eventual collapse of the
176 AMOC (Section 3c).

177
178 The main goals of the manuscript are centered around addressing these three questions:

179
180 Q1) How does a collapse of the AMOC influence the atmospheric circulation in the pres-
181 ence of the same background CO₂ forcing (SSP 2-4.5 ensemble)?

182
183 Q2) How does this compare with the response to an AMOC collapse induced by different
184 CO₂ forcing (2xCO₂ vs. 3xCO₂)?

185
186 Q3) Are AMOC-related circulation changes mediated primarily by GMST or by changes
187 in atmospheric temperature gradients?

188
189 In addressing Q1-Q3 we show that the AMOC tipping point described in AR2023 results in a
190 vastly different atmospheric response between ensemble members in which the AMOC collapses
191 versus members in which the AMOC recovers. In particular, in our model the atmospheric response
192 to an AMOC collapse (occurring on the timescales addressed in this study) reflects a regime shift
193 between a climate state in which the NH Hadley Cell and midlatitude jet are substantially weaker and

displaced further equatorward (strong AMOC), compared to a state in which they are substantially stronger and displaced poleward (weak AMOC).

2. Analysis/Methods

a. Models and Experiments

Here we use simulations from two sets of experiments produced using the GISS version E2.1 climate model (GISS-E2-1-G) (Kelley et al. (2020)), which consists of a 40-level atmospheric model with a horizontal resolution of $2^\circ \times 2.5^\circ$ latitude/longitude coupled to the 1° horizontal resolution 40-level GISS Ocean v1 (GO1) model (for more details of GO1 see AR2023). Comprehensive reviews of this model’s response to historical and future climate change simulations are provided in Miller et al. (2021) and Nazarenko et al. (2022), respectively.

We first examine results from the SSP 2-4.5 ensemble that contributed to the official submission of the NASA-GISS climate group to CMIP6. In particular, we contrast the behaviors of eight members in which the AMOC has recovered by year 2400 (SSP 2-4.5 R) with two members in which it has remained collapsed (SSP 2-4.5 C) (Fig. 1a). As discussed in AR2023, this contrasting behavior emerges during the “extension” portion following year 2090, beyond which CO_2 concentrations slow down in growth from 597 ppm to 643 ppm at year 2200 and decline thereafter (Meinshausen et al. (2020)). That study further showed that the divergence in the behavior of the AMOC results from stochastic variability associated with sea-ice transport and melting in the Irminger Sea that led to a reduction in evaporation and salinity. Note that, whereas AR2023 was primarily focused on identifying the mechanisms leading to different recovery times among the SSP 2-4.5 R ensemble members, our interest is in quantifying the impact of an AMOC collapse on the large-scale circulation after year 2400 up to year 2500. To this end, we treat the SSP 2-4.5 R and C simulations as comprising two distinct “recovered” and “collapsed” ensembles.

To put the SSP 2-4.5 results in a broader context, we also examine the coupled atmosphere-ocean 1-5x CO_2 abrupt CO_2 experiments reported in Mitevski et al. (2021), which were performed using the same version of the model. We restrict our attention to a subset of the runs, focusing mainly on the 2x CO_2 and 3x CO_2 experiments, but also including results from the 4x CO_2 and 5x CO_2 simulations when commenting on the linearity of the atmospheric circulation responses with respect to changes in GMST (Section 3b). As shown in Figure 1, the behavior of the AMOC

223 by the end of the abrupt 2xCO₂ and 3xCO₂ runs is generally very similar to the AMOC behavior
224 in the SSP 2-4.5 R and C ensemble members, respectively, past year 2400. This similar behavior
225 also appears at lower latitudes (26°N) (not shown), consistent with the findings in AR2023, who
226 showed a strong correlation in AMOC strength at these two latitudes (0.97) within the broader SSP
227 2-4.5 ensemble.

228 In addition to the results from the fully coupled ocean-atmosphere model (hereafter FOM) SSP
229 2-4.5 and XxCO₂ integrations, we also show results from q-flux or slab-ocean model (SOM)
230 integrations spanning the range 1-5xCO₂. In these experiments any changes in ocean horizontal
231 heat transport and vertical heat uptake by the deep ocean are not included as the ocean heat flux
232 convergences in the mixed layer ($-\nabla \cdot (vT)$, including both horizontal and vertical heat fluxes) are
233 calculated using preindustrial control values. At the same time, the SOM experiments do capture
234 the mixed layer temperature changes resulting from changes in the net surface heat fluxes (hereafter
235 referred to as “thermodynamic” ocean coupling). As such, contrasting the responses in the FOM
236 and SOM experiments isolates the role of dynamic (i.e., ocean heat flux convergence) coupling on
237 the atmospheric responses in the FOM simulations, consistent with the presentation in Chemke et al.
238 (2022). Note that this approach does not explicitly isolate the contribution of changes in SSTs to the
239 atmospheric circulation response, as the SST response reflects both changes in thermodynamic and
240 dynamic ocean-atmosphere coupling. However, robustly isolating the impact of SSTs can be tricky
241 as previous studies utilizing prescribed SST “warming hole” patterns have shown large sensitivity
242 to how these patterns are prescribed, particularly in relation to SST gradients (see discussion in
243 Gervais et al. (2019)).

244 *b. Temporal Averaging and Spatial Domains*

245 To compare the atmospheric responses from the SSP 2-4.5 simulations with those from the abrupt
246 CO₂ experiments we focus on climatological averaging periods during which the characteristics
247 of the AMOC are similar, i.e., years when the AMOC has recovered in the 2xCO₂ and SSP 2-4.5
248 R runs, while the AMOC has remained collapsed in the 3xCO₂ and SSP 2-4.5 C experiments.
249 As indicated in Figure 1 (dashed black vertical lines) this corresponds to years beyond which the
250 maximum value of the overturning streamfunction at 48°N has reached nearly zero, corresponding
251 to years 120-150 and 2400-2500 in the XxCO₂ and SSP 2-4.5 integrations, respectively. We refer

252 to these periods hereafter as the “equilibrated” responses in the model, bearing in mind that the
253 AMOC exhibits multi-centennial instability as was illustrated in an older version of the GISS
254 climate model (Rind et al. (2018)). Variations on these longer timescales are not addressed in this
255 study.

256 We begin by presenting differences in climatological means between the SSP 2-4.5 R and C
257 ensembles and between the 2xCO₂ and 3xCO₂ integrations. Statistical significance of the SSP
258 2-4.5 C-R differences is assessed at a confidence level of 95% using a Welch’s t-test, given the
259 unequal sample sizes represented by the 8-member R and two-member C ensembles. A two-sample
260 Student’s t-test is used when comparing the abrupt CO₂ responses. In addition, when putting the
261 SSP 2-4.5 results in the context of the broader 1-to-5xCO₂ forcing range we define all responses
262 relative to a 150-year average over the preindustrial control simulation from which the abrupt CO₂
263 experiments are “branched.”

264 For the majority of the analysis considered here we focus on December-January-February (DJF)
265 and over the NH. Our focus on DJF is consistent with the presentation in AR2023, while our
266 focus on the NH is motivated by Mitevski et al. (2021), who showed that the AMOC collapse
267 occurring between 2xCO₂ and 3xCO₂ results in a non-monotonic response in global mean surface
268 temperature, driven primarily by changes occurring in the NH (more precisely, the North Atlantic).
269 We deviate from this convention, however, at two different points in this study. First we use annual
270 mean GMST when evaluating the dynamical sensitivity scaling in Section 3b; second, we present
271 the energy budget analysis in Section 3c using annual means in order to facilitate comparison with
272 previous studies. Some results about the Southern Hemisphere (SH) circulation response are also
273 presented, but only discussed briefly.

274 Finally, while our main focus is on the “equilibrated” responses defined above, we are also
275 interested in exploiting the evolution of the responses, as in Grise and Polvani (2017) and Chemke
276 and Polvani (2019). As shown in those studies, consideration of the response timescales of different
277 variables affords insight into possible mechanisms governing their evolution.

278 *c. Scaling with Global Mean Surface Temperature (GMST)*

279 We begin by comparing the absolute differences in the atmospheric “equilibrated” responses
280 between the SSP 2-4.5 R and C members (Section 3a1-2) and between the 2- and 3xCO₂ simulations

(Section 3a3). When interpreting these differences, however, it is important to note that these could partly be reflective of background differences in the CO₂ forcing. In particular, the CO₂ values in the SSP 2-4.5 extended experiments peak at 643 ppm, or roughly 2.4 times preindustrial values, and decrease thereafter (Figure 2a in AR2023). It is perhaps not surprising, therefore, that this value of CO₂ lies in between the 2xCO₂ and 3xCO₂ levels identified in Mitevski et al. (2021) as the transition point between the AMOC recovering and collapsing under abrupt CO₂ forcing (Fig. 1b).

Given these differences in CO₂ forcing (further exaggerated when considering the broader suite of 1-5xCO₂ experiments) it may seem most natural to compare the simulations with respect to their associated instantaneous radiative forcing (RF) as in Mitevski et al. (2021). However, another difference between the transient SSP 2-4.5 and abrupt 1-5xCO₂ experiments is the evolution of the forcing. As the AMOC is known to be sensitive to the time history of the forcing, this is important to take into consideration, and so we cast our scaling analysis in Section 3b (in which the SSP 2-4.5 results are compared against the broader 1-5xCO₂ suite) in terms of GMST. This approach is also more in spirit with Ceppi et al. (2018) as it directly addresses the extent to which the dynamical sensitivity captured in the simulations scales with equilibrium climate sensitivity (Q3).

Finally, a related but distinct approach is to normalize by annual mean GMST. KB2021 showed that doing so highlights large differences in temperature gradients and the zonal mean meridional circulation between models in which the AMOC weakens substantially (> 7 Sv), compared to models showing a limited AMOC response (< 7 Sv). However, while this approach is well suited to understanding the multi-model response to the same (4xCO₂) forcing, it does not directly afford insight into how dynamical sensitivity scales with GMST. As we have tried both normalizing and not normalizing in this study and draw generally very similar conclusions (not shown), we focus on the unnormalized results.

d. Analysis Approach

1) HADLEY CELL AND STORM TRACK DIAGNOSTICS

Whereas KB2021 focused on the latitude of the northern midlatitude jet, here we expand their analysis to also include measures of the Hadley Cell (hereafter HC) and the storm tracks. Figure 2a

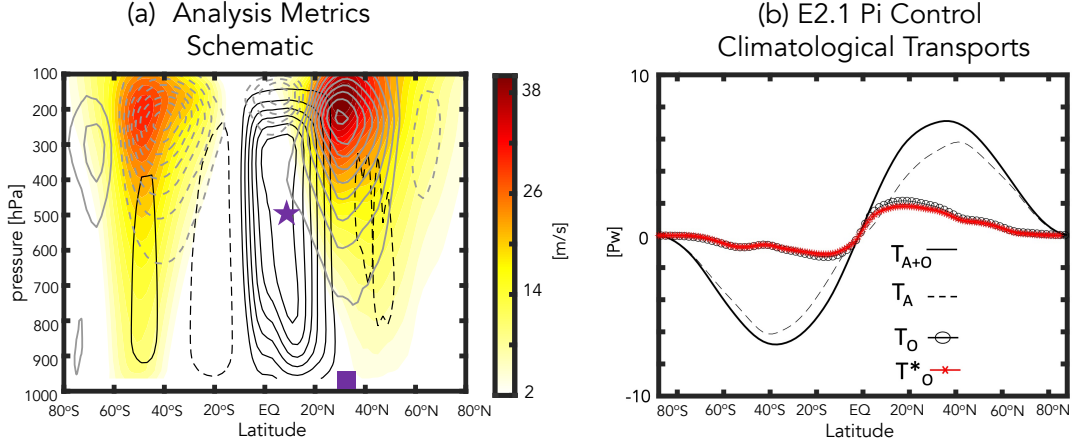


FIG. 2. (a): Schematic of the main zonal mean dynamical metrics considered in this study, illustrated using data from the preindustrial control simulation. The December-January-February (DJF) climatological mean meridional circulation is shown in black contours, with solid and dashed lines denoting clockwise and counterclockwise directions, respectively (contour interval: 3×10^{10} kg/s). The DJF zonally averaged zonal winds are shown in the filled colored contours (only positive values shown; contour interval: 2 m/s) and the DJF eddy momentum fluxes are shown in the grey contours (contour interval: $8 \text{ m}^2/\text{s}^2$). The purple star denotes the Northern Hemisphere (NH) HC strength, or the maximum value of the mean meridional streamfunction at 500 hPa equatorward of where it crosses zero, while the edge is denoted by ϕ_{UAS} (purple square), or the zero-crossing latitude of the surface zonal wind. (b): Annual mean meridional distributions of the total atmospheric (T_A ; black dashed line) and combined atmosphere-ocean (T_{A+O} ; black solid line) northward energy transports for the preindustrial control simulation. The implied ocean heat transport (T_O ; black circled line), calculated by subtracting T_A from T_{A+O} , exhibits good agreed with online calculations of the ocean transports (T_O^* ; red starred line). For more details see Section 2.

highlights how these measures of the HC and midlatitude jet are coupled through eddy momentum fluxes.

To quantify the characteristics of the HC we use metrics calculated using the Tropical-width Diagnostics (TropD) code (Adam et al. (2018)) based on fields that were zonally and seasonally

326 averaged before calculation of the metrics. The edge of the HC, ϕ_{UAS} , is defined as the zero-crossing
 327 latitude of the surface zonal wind (corresponds to UAS in TropD and is calculated using the “zero-
 328 crossing” method) (Fig. 2a, purple square). Our use of a surface-wind based measure of the HC
 329 edge is partly motivated by previous studies showing a strong signature of an expanded northern
 330 edge of the HC on sea level pressure (SLP) (Schmidt and Grise (2017)). This measure of the HC
 331 was also shown to correlate well with the latitude at which the mean meridional streamfunction
 332 at 500 hPa crosses 0 poleward of its tropical extremum (Waugh et al. (2018)). The value of that
 333 tropical extremum (Ψ_{500}) is also examined as a measure of HC strength (Fig. 2a, purple star).

334 In addition to looking at the HC, we also examine its relation to the northern midlatitude jet via
 335 the eddy momentum fluxes. This is based on research showing a strong connection between the
 336 evolution of the HC and the latitude of the maximum eddy momentum fluxes (Schneider (2006);
 337 Chemke and Polvani (2019); Menzel et al. (2019)). The eddy momentum fluxes are calculated
 338 as in Chemke and Polvani (2019) as the time mean of $[u'v']$, where u and v are the zonal and
 339 meridional winds, respectively, and primes represent deviations from both the zonal and monthly
 340 means. In particular we are interested in the latitude where the eddy momentum flux maximizes
 341 (eddy momentum convergence = 0) (Fig. 2a, grey contours). As it is well known that the largest
 342 eddy momentum flux convergences are closely collocated with the extratropical storm tracks (e.g.,
 343 Lau et al. (1978), Lim and Wallace (1991)), we also examine the vertically averaged eddy kinetic
 344 energy, calculated using daily output. Connections with static stability (S_p) and baroclinic eddy
 345 generation are also made, where $S_p = -(\frac{T}{\theta})(\frac{\partial \theta}{\partial p})$ and θ is potential temperature. The baroclinic
 346 eddy generation is quantified using $\sim \alpha' \omega'$, where primes denote zonal deviations and α and ω refer
 347 to one over the density and vertical velocity in pressure coordinates, respectively (Lorenz (1955)).

348 2) ENERGETIC ANALYSIS

349 To put the results of the dynamical analysis in an energetic context we evaluate the total meridional
 350 heat transport of the coupled ocean-atmosphere transport system, further partitioned into its oceanic
 351 and atmospheric contributions. Following Magnusdottir and Saravannan (1999) we estimate the
 352 total vertically integrated atmospheric heat flux (T_A) as:

$$\frac{\partial \cos \phi}{a \cos \phi \partial \phi} \overline{[T_A]} \equiv \frac{\partial \cos \phi}{a \cos \phi \partial \phi} \int_1^0 \overline{(c_p T + g z + L q) v \rho d \eta}$$

$$= \overline{[-F_T - F_S + SHF + LHF]} \quad (1)$$

as well as the vertically integrated meridional heat flux in the combined atmosphere-ocean system (T_{A+O}) as:

$$\frac{\partial \cos \phi}{a \cos \phi \partial \phi} \overline{[T_{A+O}]} \equiv \overline{[-F_T]} \quad (2)$$

where moist static energy density is the sum of dry static energy density ($c_p T + gz$) and the latent heat density (Lq), ρ and v refer to the mass density and horizontal velocity on η surfaces. Zonal averages and time averages are denoted by square brackets and overbars, respectively. The terms on the RHS of both equations refer to energy fluxes out of the top of the atmosphere and at the surface: F_T (net upward flux of radiation at the top of the atmosphere, calculated as outgoing longwave radiation (OLR) minus the absorbed solar radiation (ASR)), F_S (net downward flux of radiation at the surface equal to the sum of net downward longwave (LWF) and shortwave (SWF) radiation), and the fluxes of latent and sensible heat at the surface (LHF and SHF).

The resulting annual mean meridional distributions of T_A and T_{A+O} , calculated using the E2.1 150-year preindustrial control simulation, is consistent with the climatological energy transports presented in other studies (e.g., Magnusdottir and Saravannan (1999), Held and Soden (2006)) (Figure 2b). Note that the implied ocean heat transport, calculated by subtracting the first from the second equation above (Fig. 2b, black circled line) is found to exhibit good agreement with online calculations of the ocean transports (Fig. 2b, red starred line). These northward ocean heat transports, simulated in historical integrations using E2.1, have been shown to agree well with 1992-2011 estimates from the ECCO ocean state estimate (Figure 23 in Kelley et al. (2020)). Finally, in addition to examining the compensation between atmospheric and oceanic poleward transports, we also further partition T_A into its moist versus dry contributions using online calculations of the vertically integrated dry static energy and latent heat northward transports (Section 3c).

3. Results

We begin by contrasting the regional SSP 2-4.5 C and R responses in sea surface temperature, sea level pressure, precipitation and zonal winds (Section 3a1) and in the large-scale zonal mean

circulation (Section 3a2). Then we compare the SSP 2-4.5 C-R differences to the responses in the 2xCO₂ and 3xCO₂ simulations (Section 3a3), followed by a discussion of the full set of abrupt 1-5xCO₂ experiments, which we use to examine how the changes in thermodynamics and the circulation scale with changes in global mean surface temperature (Section 3b). To interpret the dynamical scaling results we then examine the compensation that arises between the ocean and atmosphere in response to a decline and eventual collapse of the AMOC (Section 3c).

a. Equilibrated Responses

1) SSP 2-4.5 COLLAPSED VS. RECOVERED: SEA SURFACE TEMPERATURES, PRECIPITATION, SEA LEVEL PRESSURE AND WINDS

Figure 1 (bottom panels) shows the evolution of annual global mean surface temperature in the SSP 2-4.5 C and R members (Fig. 1c) and the abrupt CO₂ experiments (Fig. 1d). Comparing the collapsed versus recovered SSP 2-4.5 ensemble members reveals global cooling associated with a sustained collapse of the AMOC such that by the time that the AMOC has recovered in the SSP 2-4.5 R members the annual mean global surface temperature is almost one degree warmer, relative to the SSP 2-4.5 C members. In the abrupt CO₂ simulations, the GMST change in the 3xCO₂ experiment is only ~0.6°C warmer than the 2xCO₂ simulation, reflective of a clear flattening of the warming trend after years ~60-70. Overall, the changes in GMST are 2.2°C, 2.8°C, 3.0°C, and 2.3°C for the 2xCO₂, 3xCO₂ and SSP 2-4.5 recovered and SSP 2-4.5 collapsed ensembles, respectively.

That the cooling associated with a steady decline and eventual collapse of the AMOC acts to mitigate, and partially counteract, other components of the global surface temperature change is reflected in a non-monotonic change in equilibrium climate sensitivity that occurs between 2xCO₂ and 3xCO₂ over the broader range of experiments spanning 1-to-5xCO₂ (Figure 1 in Mitevski et al. (2021)). This counteracting of warming due to a weakening of the AMOC has also been shown to occur in 21st century warming simulations (Drijfhout et al. (2012), Caesar et al. (2018), Marshall et al. (2015)).

While the AMOC influence on the climate can occur via its changes in GMST, a reduction in AMOC strength can also influence sea surface temperature patterns. We examine this next, with a focus on DJF, and examine changes in SSTs and associated spatial gradients over the Atlantic and

Pacific (Figure 3a). Note that a saturated color bar has been used in order to highlight the structure of SST changes outside of the North Atlantic region.

Examination of the North Atlantic reveals much more cooling in the SSP 2-4.5 collapsed simulations (Fig. 3a) over the subpolar North Atlantic (SPNA), consistent with the results from previous studies. This cooling within the SPNA region is also associated with a large increase in meridional SST gradients over the North Atlantic south of 40°N and enhanced zonal gradients between the western and eastern Atlantic basins. There is also an indication of a slight increase in SST gradients in the tropics.

The cooler SSTs in the collapsed simulations are not only confined to the Atlantic, but also span the Pacific (Fig. 3a), resulting in stronger meridional SST gradients, particularly over middle northern latitudes. Preliminary analysis of the evolution of the SST response (Appendix Figure 1) shows that this cooling over the extratropical Pacific occurs over several centuries and may be related to a deepening and poleward shift of the Aleutian Low (Fig. 3c), resulting in more advection of colder temperatures over the West Pacific (Wu et al. (2008)), although direct thermodynamic advection of colder North Atlantic air may also be occurring. By comparison, the changes in SSTs and associated gradients in the tropical Pacific are much smaller. Unlike some previous studies (Timmermann et al. (2007), Zhang and Delworth (2005)) we find no evidence of an El Niño like response to an AMOC weakening, although the robustness of this response has recently been questioned (KB2021).

In the SH, SSTs warm over the extratropics in the SSP 2-4.5 collapsed integrations, compared to the simulations in which the AMOC recovers. This warming takes several centuries to develop (Appendix Figure 1) and resembles the evolution of the SST pattern documented in Pedro et al. (2018) (their Figure 7). This delayed warming over the SH results in increased SST gradients over the South Atlantic (~60°S) in the SSP 2-4.5 C runs, relative to SSP 2-4.5 R, a feature which is not captured in the 3xCO₂ simulation (discussed more in Section 3a3).

In addition to the changes in SSTs, the response in precipitation in the SSP 2-4.5 collapsed simulations reflects large decreases over the North Atlantic subpolar region, reductions over the Amazon and suggestions of a southward shift of the ITCZ over both the Atlantic and East Pacific basins (Fig. 3b). By comparison, the increased precipitation in the West Pacific is not statistically significant, consistent with previous studies (Vellinga and Wood (2008), KB2021).

Moving next to more dynamical measures, we examine changes in sea level pressure and near-surface zonal winds (Fig. 3c,d). The changes in SLP show differences over the North Atlantic indicative of enhanced (anticyclonic) high level pressure over the subpolar latitudes in the runs in which the AMOC collapses (Fig. 3c). This increase in SLP is shifted slightly downstream of the SST changes, as noted in Gervais et al. (2019), albeit for the prescribed SST experiments examined in that study. In addition to the changes over the Atlantic, there is also a pronounced dipole of increased and reduced sea level pressure values over the North Pacific middle and high latitudes. While this response was not discussed in KB2021, earlier studies have shown that a weakening of the AMOC is associated with a deepening of the Aleutian Low (Wu et al. (2008), Liu et al. (2020)).

Consistent with the SLP changes over the North Pacific, there is a strong signature of a weakened AMOC in the near surface zonal winds (850 hPa) (Fig. 3d). These wind changes over the Pacific reflect a poleward shift of the midlatitude jet, whereas over the North Atlantic the jet mainly accelerates and extends further eastward over Europe. This acceleration over the North Atlantic is more pronounced in the mid-troposphere (Fig. 3e), as was also reported in KB2021, who identified a statistically significant strengthening of the midlatitude jet at 250 hPa, but not at 850 hPa, in models featuring a stronger AMOC decline. Finally, in contrast to the NH, there is a uniform weakening of the zonal winds over the SH extratropics. We discuss the vertical coherence of these wind changes in the next section.

2) SSP 2-4.5 COLLAPSED VS. RECOVERED: VERTICAL STRUCTURE

In addition to its impacts on SSTs, changes in the AMOC impact the vertical structure of meridional temperature gradients in the atmosphere. To interpret the zonal wind changes shown in Figure 3 we therefore next examine the zonal mean changes in temperatures, zonal winds and eddy kinetic energy, as well as their coupling to responses in the tropical mean meridional circulation (Figure 4).

We begin by examining changes in temperature (Fig. 4a), which show much more cooling over the NH high latitude troposphere in the SSP 2-4.5 collapsed runs. A similar reduction in Arctic warming was reported in the “strongly” collapsed models examined in KB2021 (their Figure S5) and in Liu et al. (2020) (their Figure 6). In addition to the changes over the northern extratropics, we also find an indication of weak polar amplification in the SH characterized by warming throughout

SSP 2-4.5 Collapsed - Recovered

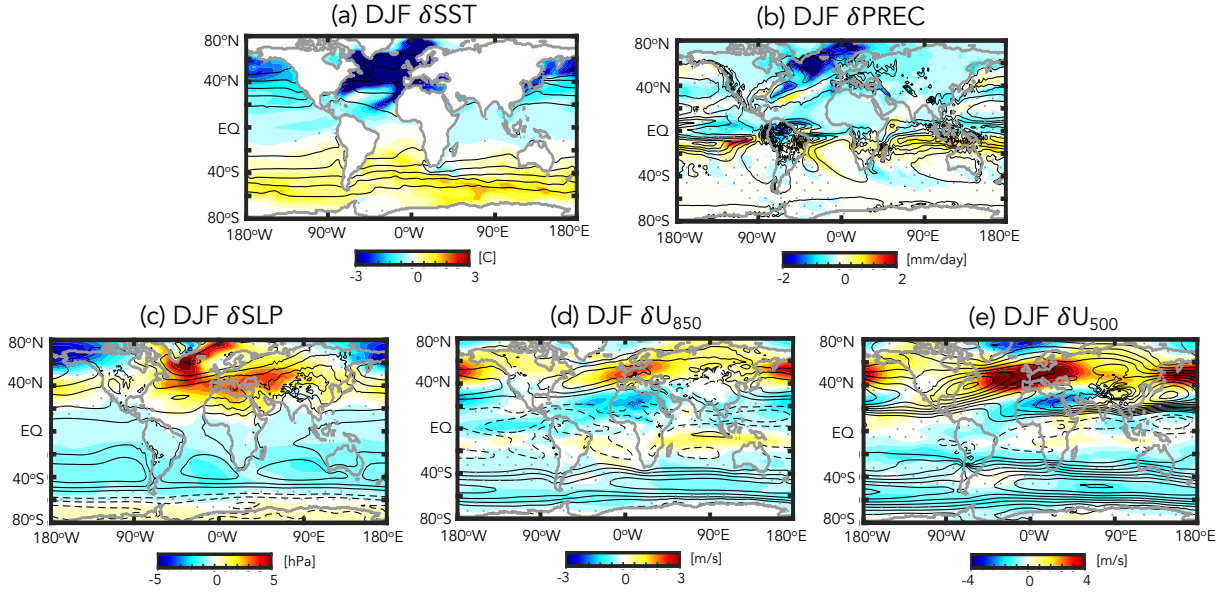


FIG. 3. The difference in the year DJF 2400-2500 climatological mean (a) sea surface temperatures (δ SST), (b) precipitation (δ PREC), (c) sea level pressure (δ SLP), (d) 850 hPa zonal winds (δ U₈₅₀) and (e) 500 hPa zonal winds (δ U₅₀₀) between the SSP 2-4.5 collapsed (C) and recovered (R) ensemble members. Climatological mean values from the preindustrial control simulation are denoted in the black contours (contour intervals: (a) 5°C, (b) 2 mm/day, (c) 5 mb, (d) 3 m/s and (e) 3 m/s). Grey stippling denotes regions where the SSP 2-4.5 C-R differences are not statistically significant.

the SH middle and high latitudes poleward of 40°S, also seen in the SST differences (Fig. 3a). This warming in the SH is consistent with Liu et al. (2020) (their Figure 6), but inconsistent with KB2021, which likely reflects their focus on shorter (100-150 year) timescales. In addition, KB2021 also identified more warming in the tropical upper troposphere, a feature that is also not evident in the SSP 2-4.5 collapsed runs. Normalization of our results by GMST (not shown) produces an anomalous upper tropical tropospheric warming, suggesting that the results reported in KB2021 are reflective of the normalization performed in that study, not of absolute temperature differences.

Moving next to the zonal winds (Fig. 4b) we find that the reduced warming over NH high latitudes is associated with enhanced meridional temperature gradients, which result in a poleward

SSP 2-4.5 Collapsed - Recovered

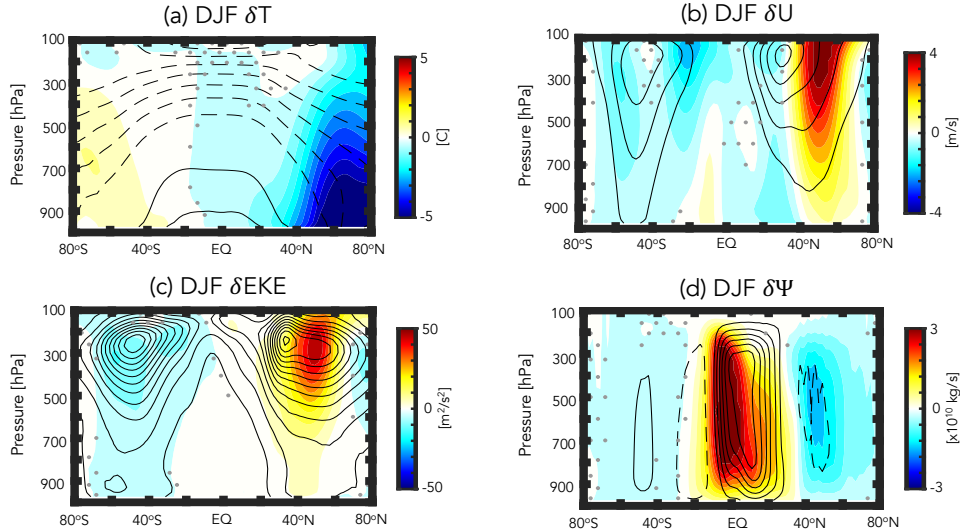


FIG. 4. The difference in the year DJF 2400-2500 climatological mean zonal mean (a) temperature (δT), (b) zonal wind (δU), (c) eddy kinetic energy (δEKE) and (d) Eulerian mean streamfunction ($\delta \Psi$) between the SSP 2-4.5 collapsed (C) and recovered (R) ensemble members. Climatological mean values from the preindustrial control simulation are denoted in the black contours (contour intervals: (a) 10°C , (b) 8 m/s , (c) $28\text{ m}^2/\text{s}^2$ and (d) $3 \times 10^{10}\text{ kg/s}$). Note that in (d) solid and dashed lines denoting clockwise and counterclockwise directions, respectively. Grey stippling denotes regions where the SSP 2-4.5 C-R differences are not statistically significant.

shift of the zonal mean northern midlatitude jet in response to a decline and eventual collapse of the AMOC. A similar poleward shift in the NH jet was documented in KB2021 (their Figure 4) and in Liu et al. (2020). In the SH the zonal winds weaken and, if anything shift equatorward, in the SSP 2-4.5 C ensemble members, consistent with the weak polar amplification in that region (Fig. 4a). Again, this wind response is highly consistent with Liu et al. (2020), but opposite to that shown in KB2021, who identified a poleward shift of the SH jet. As that study did not propose a testable mechanism for the SH jet changes, it is not entirely clear what is the driver of the differences between their results and those presented here and in Liu et al. (2020), although both the normalization by GMST as well as the differing integration lengths likely contribute.

In concert with the changes in the zonal winds, the changes in eddy kinetic energy (EKE) over the NH feature increases north of 40°N (Fig. 4c). Note that there is no statistically significant

DJF Eddy Kinetic Energy

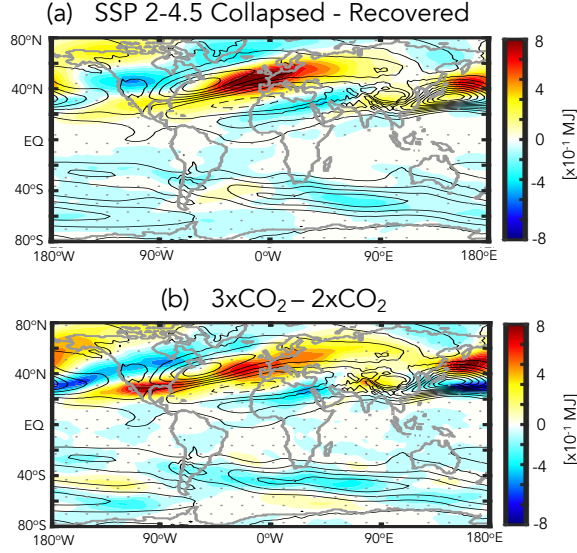


FIG. 5. (a) The difference in the year DJF 2400-2500 climatological mean vertically integrated eddy kinetic energy between the SSP 2-4.5 C and R ensembles. (b) Same as in (a), except showing the year 120-150 difference between the $3\times\text{CO}_2$ and $2\times\text{CO}_2$ integrations. Climatological mean values from the preindustrial control simulation are denoted in the black contours (contour interval: 5×10^{-1} MJ).

response in the subtropics and only the wind (and EKE) changes poleward of 40°N are robust. Zonally, the increases in EKE are concentrated over the North Atlantic and extend eastward over Europe, as well as over the West Pacific (Fig. 5a), strongly resembling the zonal wind changes at 500 hPa (Fig. 3e). Comparisons with the changes in EKE associated with an AMOC collapse in another model (the Community Earth System Model (CESM-LE)) examined in Mitevski et al. (2021) show very similar anomalies (not shown). Furthermore, a spectral decomposition of these NH EKE changes show increased wave energy over zonal wavenumbers 1-6 in the collapsed SSP 2-4.5 members, relative to the recovered members (also not shown).

Finally, the changes in the mean meridional streamfunction indicate an overall strengthening of the wintertime NH Hadley circulation in the collapsed SSP 2-4.5 simulations (Fig. 4d). This intensification of the NH Hadley circulation in response to an AMOC shutdown has been reported in previous studies (Zhang and Delworth (2005), Orihuela-Pinto et al. (2022)) and generally associated with a southward displacement of the ITCZ, although Brayshaw et al. (2009) also identify a zonally localized enhancement of the HC region over the subtropical Atlantic, which

$$3\times\text{CO}_2 - 2\times\text{CO}_2$$

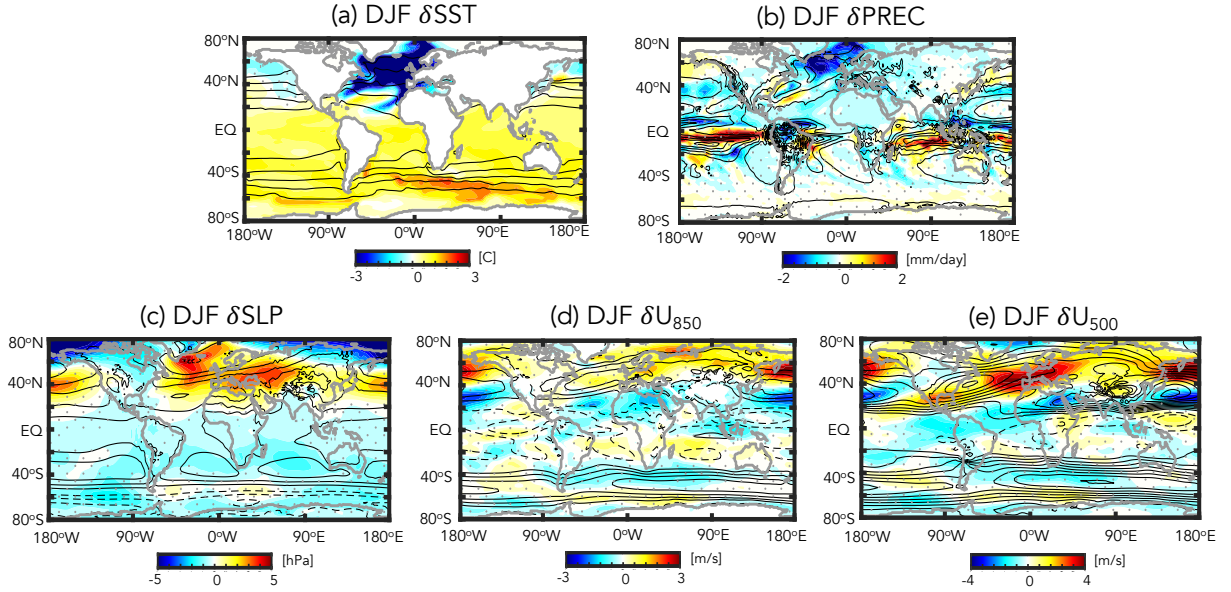


FIG. 6. Same as Figure 3, except showing the difference between the year 120-150 climatological mean $3\times\text{CO}_2$ and $2\times\text{CO}_2$ responses.

they associate with increased meridional SST gradients in that region. Compared to those studies, however, our results also show a poleward displacement of the northern HC edge in the lower troposphere (>500 hPa), a result which has not been directly commented on in the literature. These streamfunction anomalies over the NH extratropical lower troposphere appear to be coupled to a slight strengthening and poleward displacement of the northern Ferrel cell.

3) COMPARISON WITH $2\times\text{CO}_2$ vs $3\times\text{CO}_2$

Comparisons of the surface and lower tropospheric impacts associated with an AMOC collapse in the SSP 2-4.5 ensemble (Fig. 3) are highly consistent with the responses moving from $2\times\text{CO}_2$ to $3\times\text{CO}_2$ (Fig. 6). In particular, over the North Atlantic the changes moving from $2\times\text{CO}_2$ to $3\times\text{CO}_2$ reflect cooler SSTs (Fig. 6a), reduced precipitation (Fig. 6b) and an anomalous anticyclonic circulation over the North Atlantic subpolar gyre region (Fig. 6c), as well as a strengthening and eastward extension of the North Atlantic jet over Europe (Fig. 6d, 6e). The magnitudes of the

530 3xCO₂ changes are also similar to the responses in the SSP 2-4.5 collapsed ensemble members,
531 albeit somewhat smaller (Fig. 3).

532 Though the overall responses in the surface temperatures and winds are very similar, there are
533 some important differences worth noting. First, the SSTs in the 3xCO₂ simulation show much less
534 cooling over the Pacific northern midlatitudes (> 40°N) compared to the SSP 2-4.5 C simulations,
535 which likely reflects differences in the length of these integrations as this cooling takes centuries
536 to equilibrate (Appendix Figure 1). Second, in response to 3xCO₂ there is more warming over the
537 NH subtropics and tropics, consistent with the higher CO₂ forcing in that simulation. Thus, unlike
538 what happens in the SSP 2-4.5 C ensemble members, there is no SH polar amplification occurring
539 at 3xCO₂.

540 The different SST gradients over the northern high latitude Pacific and tropics and SH occurring
541 at 3xCO₂ have implications for the jet and precipitation changes in these regions. In particular,
542 over the Pacific northern midlatitudes, where there is much less cooling compared to the SSP 2-4.5
543 C integrations, the jet response resembles more of a poleward shift, characterized not only by an
544 acceleration north of 40°N, but also reduced winds ~20°N; in the tropical Pacific there is also a
545 much stronger increase in precipitation, relative to the AMOC SSP 2-4.5 C ensemble.

546 Even over the North Atlantic the SST cooling is slightly weaker and less expansive and the jet
547 response at 850 hPa is not statistically significant at 3xCO₂, in contrast to the SSP 2-4.5 collapsed
548 ensemble members. In the SH, there is also a suggestion of a poleward shift of the midlatitude jet
549 at 3xCO₂, not evident in the SSP 2-4.5 C integrations, although these changes are not statistically
550 significant. These subtle differences aside, however, the overall similarities between Figures 3 and
551 6 are remarkable and suggest that the climate response that occurs moving from 2xCO₂ to 3xCO₂
552 is, to first order, determined by the changes in AMOC strength.

553 Strong consistency is also found when comparing the vertical response of the large-scale circula-
554 tion between the AMOC SSP 2-4.5 C and R ensemble members (Fig. 4) and between the 3xCO₂
555 and 2xCO₂ integrations (Fig. 7). That is, in concert with stronger cooling over the Arctic (Fig.
556 7a), the 3xCO₂ simulation features a stronger poleward shift of the NH zonal mean jet (Fig. 7b),
557 increased EKE northward of 40°N (Fig. 7c) and a strengthened HC (Fig. 7d).

558 One difference in vertical structure occurs over the Arctic, where the cooling that occurs at
559 3xCO₂ (Fig. 7a) is much smaller than in the collapsed SSP 2-4.5 ensemble (Fig. 4a), reflecting

$$3\times\text{CO}_2 - 2\times\text{CO}_2$$

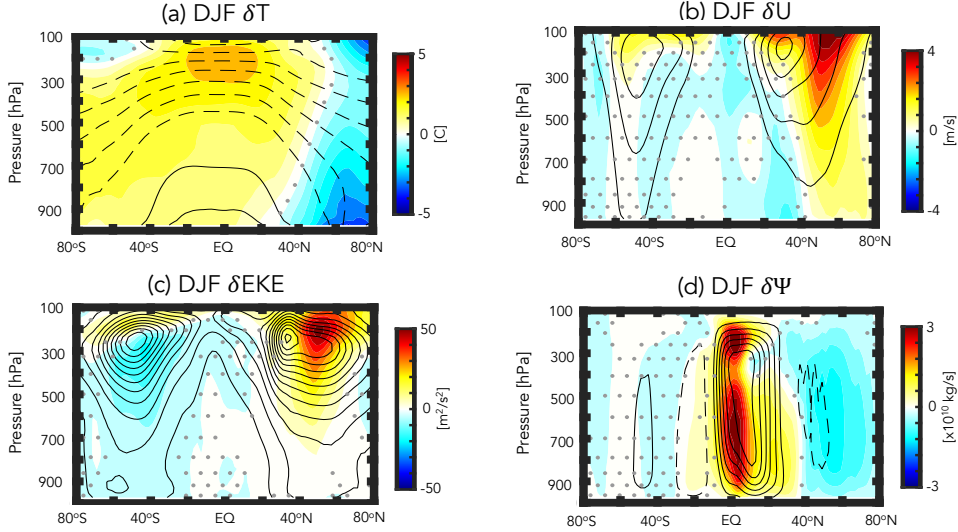


FIG. 7. Same as Figure 4, except showing the difference between the year 120-150 climatological mean $3\times\text{CO}_2$ and $2\times\text{CO}_2$ responses.

the higher CO_2 forcing in that simulation. There is also stronger warming occurring within the tropics and over southern latitudes. Despite these differences in absolute temperature, however, the increase in meridional temperature gradients that occurs is similar to what happens when comparing the SSP 2-4.5 C and R ensemble members. As such, the zonal mean NH jet response to an AMOC collapse is quite similar in the $3\times\text{CO}_2$ simulation (Fig. 7b) compared to SSP 2-4.5 C (Fig. 4b) and is also coupled to an EKE increase on the poleward flank of the jet (Fig. 7c). Maps of the EKE response show that at $3\times\text{CO}_2$ much of this increased EKE reflects changes over the Atlantic (Fig. 5b), as in the SSP 2-4.5 C ensemble (Fig. 5a), although there is also increased EKE over the western Pacific and North America.

To summarize: In response to a collapse of the AMOC, our results show widespread cooling over the Arctic and stronger meridional temperature gradients over the NH. This increase in temperature gradients is associated with a poleward shift of the midlatitude jet (and associated eddy energy) as well as a strengthening of the NH HC. In the lower troposphere (> 600 hPa) the NH HC is displaced poleward.

Over the Northern Hemisphere the response to an increase from $2xCO_2$ to $3xCO_2$ is remarkably similar to the differences between the SSP 2-4.5 R and C simulations, in terms of both the magnitude and spatial patterns of these changes. Some exceptions, however, include the near surface (850 hPa) wind response over the North Atlantic, which is not statistically significant at $3xCO_2$, as well as in the tropics, where precipitation increases strongly over the Pacific. There is also more warming in the tropical upper troposphere and SH in the $3xCO_2$ simulation. Overall, this close correspondence suggests that the collapse of the AMOC is the dominant driver of the large-scale circulation changes moving from $2xCO_2$ to $3xCO_2$ in our model.

b. Scaling of Equilibrated Thermodynamic and Dynamic Responses with Global Mean Surface Temperature (GMST)

One question (Q3) not addressed in the previous sections relates to how changes in the climate response to an eventual collapse of the AMOC scale with changes in GMST. To this end, here we expand our analysis to include the results of additional ($4xCO_2$ and $5xCO_2$) FOM abrupt CO_2 runs, as well as the results from the SOM abrupt CO_2 integrations.

1) GLOBAL THERMODYNAMIC CHANGES

Figure 8a shows the annual global mean surface temperature response among all of the simulations, plotted as a function of associated instantaneous radiative forcing (RF), where RF is calculated from the expression $5.35\ln(NxCO_2/1xCO_2)$ (Byrne and Goldblatt (2014)) and, for each run, N is the CO_2 multiple of the PI value (2.4, for the case of all SSP 2-4.5 ensemble members). The changes in GMST across this broader range of CO_2 forcing show the nonlinear behavior between the $2xCO_2$ and $3xCO_2$ FOM simulations (blue circles) that was first identified in Mitevski et al. (2021) (their Figure 1). By comparison, the results from the SOM experiments (aqua circles) show no evidence of a nonlinearity. This result was also documented in Mitevski et al. (2021) and suggests that the changes in ocean horizontal and vertical heat fluxes not included in the q-flux experiments are primarily responsible for the nonlinear changes in GMST occurring in the FOM experiments.

Building on Mitevski et al. (2021), here we also include the results from the SSP 2-4.5 R and C ensemble members (red circles, cyan and blue outlines) which are seen to align respectively with the

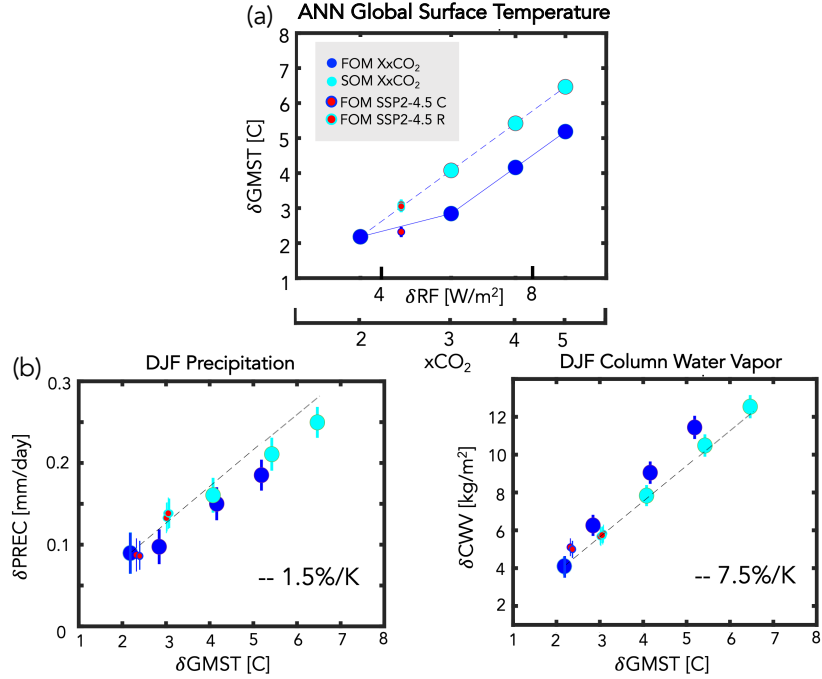


FIG. 8. Top: Changes in annual mean global mean surface temperature (GMST), plotted as a function of the associated radiative forcing (RF), calculated from the expression $5.35\ln(Nx\text{CO}_2/1x\text{CO}_2)$ (Byrne and Goldblatt (2014)) where, for each run, N is the CO₂ multiple of the PI value (2.4, for the case of the SSP 2-4.5 ensemble members), consistent with the presentation in Mitevski et al. (2021). Bottom: Changes in DJF global mean precipitation (left) and atmospheric column water vapor (right). Changes in precipitation and column water vapor are plotted relative to the annual mean GMST changes in (a). Results from the abrupt 2-5xCO₂ fully coupled atmosphere-ocean model (FOM) and slab ocean model (SOM) results are shown in the blue and cyan filled circles. The FOM SSP 2-4.5 recovered (R) and collapsed (C) results are also shown in the red circles (cyan and blue outlines, respectively). Interannual variability for each metric is indicated by the vertical bars. Note that in all panels the SOM 2xCO₂ results have been adjusted to match the FOM 2xCO₂ results in order to facilitate comparison of the FOM and SOM scalings with CO₂ and GMST, not on the absolute magnitude of the responses.

SOM (solid cyan) and FOM (solid blue) scalings. This suggests that the GMST differences between the collapsed (C) versus recovered (R) SSP 2-4.5 ensemble members are primarily associated with the changes in ocean heat convergence occurring in the former. Note that the SSP 2-4.5 results are plotted with respect to the peak CO₂ level achieved (i.e. 643 ppm), which occurs at year 2200 (not

at the values occurring during years 2400-2500, which are lower (579-598 ppm)) (Meinshausen et al. (2020)).

Next we examine how changes in first-order thermodynamic variables scale with these (nonlinear) changes in GMST. As with GMST, the changes in global mean precipitation and integrated column water vapor (CWV) also vary nonlinearly with respect to radiative forcing in the FOM simulations moving from $2\times\text{CO}_2$ to $3\times\text{CO}_2$ (Appendix Figure 2). As expected from the GMST changes, this behavior is absent in the SOM integrations and the SSP 2-4.5 C and R members again align with the FOM and SOM scalings, respectively. However, plotting the precipitation and CWV DJF changes relative to annual mean GMST, reveals that the nonlinear scaling with RF more-or-less disappears (Fig. 8b). This demonstrates that, while the first order global scale hydrological cycle is sensitive to the collapse of the AMOC, this sensitivity occurs primarily through changes in GMST.

Finally, we note that the scaling of precipitation and CWV with GMST roughly follow the predictions from Held and Soden (2006), who identified a Clausius-Clapeyron (CC) scaling of integrated column water vapor (dashed black line denoting 7.5%/K, Fig. 8b, right) and a significantly sub-CC scaling of global mean precipitation (1.5%/K, Fig. 8b, left). While some additional nonlinearity in precipitation is also evident at higher CO_2 levels, as this is not immediately relevant to the SSP 2-4.5 ensemble, we reserve further discussion for future work.

2) NORTHERN HEMISPHERE DYNAMICAL CHANGES: A REGIME SHIFT

Moving next to the dynamical response, we find that several measures of the NH DJF zonal mean dynamical circulation behave nonlinearly (and even non-monotonically) with respect to radiative forcing in the FOM simulations (Appendix Figure 3). Unlike precipitation and CWV, however, this non-linear behavior in the NH surface wind-based HC edge (Fig. 9a), HC strength (Fig. 9b), northern midlatitude EKE (Fig. 9c), latitude of maximum eddy momentum fluxes (Fig. 9d) and northern subtropical static stability (Fig. 9e) also occurs after plotting as a function of GMST. Overall, these results suggest that there is no clear (certainly not linear) relationship between the responses in the northern HC (strength and lower tropospheric edge) and midlatitude jet and changes in GMST in simulations ($>3\times\text{CO}_2$ and SSP 2-4.5 C) in which the AMOC eventually collapses.

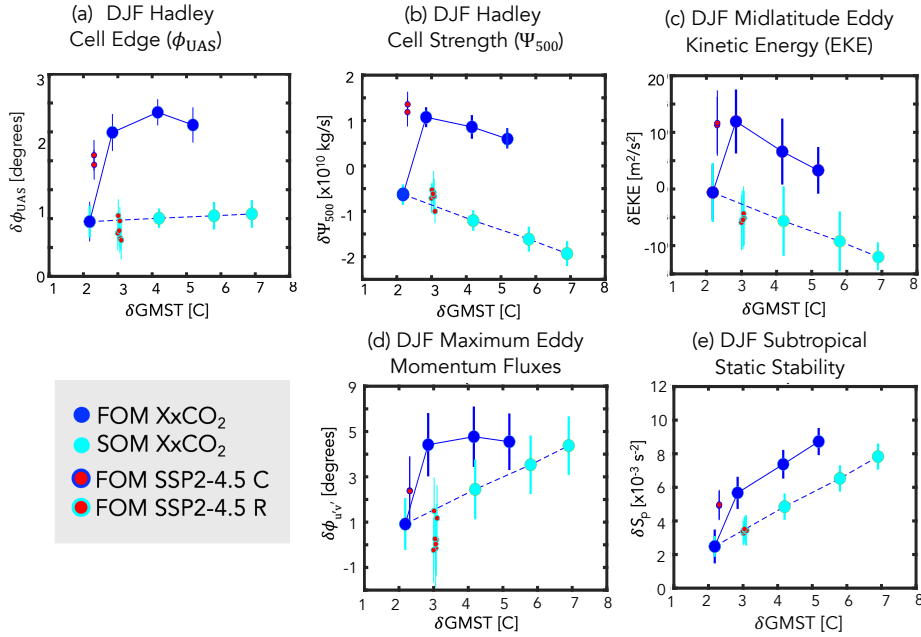


FIG. 9. Changes in various DJF Northern Hemisphere (NH) dynamical metrics, plotted as a function of GMST. Specifically, shown are the HC edge (ϕ_{UAS}) (a), HC strength (Ψ_{500}) (b), NH column eddy kinetic energy (EKE) (c), latitude of the maximum NH eddy momentum fluxes (d) and NH subtropical dry static stability (e). The quantities in (a), (b) and (d) are defined in Section 2, while the zonally averaged EKE and static stability changes have both been averaged over 300-1000 hPa and over 30°N-60°N and 20°N-40°N, respectively. Results from the abrupt 2-5xCO₂ fully coupled atmosphere-ocean model (FOM) and slab ocean model (SOM) results are shown in the blue and cyan filled circles. The FOM SSP 2-4.5 recovered (R) and collapsed (C) ensemble members are shown in the red circles (cyan and blue outlines, respectively). Interannual variability for each metric is indicated by the vertical bars. As in Figure 8 the SOM 2xCO₂ results have been adjusted to match the FOM 2xCO₂ results.

Rather, the changes in the NH circulation reflect an abrupt poleward shift and increase, respectively, moving from 2xCO₂ to 3xCO₂ and between the SSP 2-4.5 R and SSP 2-4.5 C ensemble members. Furthermore, the responses in the NH HC edge, HC strength, midlatitude eddies and momentum fluxes saturate at 3xCO₂ forcing, which is indicative of a “regime” shift in our model, consistent with the use of the term in Caballero and Langen (2005), albeit for the low-gradient, high temperature regime identified in their study using a more idealized model (see discussion in Section 4). In particular, our results suggest that the AMOC collapse is associated with a regime shift in our model between a climate state in which the HC is substantially weaker and displaced

equatorward (strong AMOC) and a state in which the HC and midlatitude EKE is stronger and displaced poleward (weak AMOC).

While the HC and midlatitude eddy energy share a similar nonlinear behavior with respect to GMST, there are some important differences worth noting. In particular, whereas the HC edge (Fig. 9a) and latitude of maximum eddy momentum fluxes (Fig. 9d), saturate at $3\times\text{CO}_2$, the changes in HC strength and midlatitude EKE continue to decrease for higher CO_2 values, despite continued increases in GSMT. At the same time, the subtropical static stability changes (Fig. 9e) are monotonic and more similar in spirit to the HC edge changes, compared to the changes in midlatitude EKE. The similar behavior shared by the HC edge and momentum fluxes is consistent with recent studies showing that the HC edge is strongly linked to the latitude of maximum eddy momentum fluxes (Chemke and Polvani (2019); Waugh et al. (2018); Menzel et al. (2019)).

One might expect that an expansion of the HC due to increased subtropical static stability would also impact the extratropical tropospheric eddy response by shifting the eddy fields poleward (Chemke and Polvani (2019); Menzel et al. (2019)). While this may partly explain the response in midlatitude EKE (Fig. 9c), however, the decreases in EKE that occur for CO_2 values higher than $3\times\text{CO}_2$ suggest that other processes are also at play. In particular, further investigation of the EKE changes reveals that the increased generation of baroclinic eddies occurs in the region of strongest zonal vertical wind shear (Fig. 4b, Fig. 7b), where, if anything, static stability increases (not shown). This enhanced baroclinity over northern midlatitudes is therefore also reflective of the strong mid-tropospheric meridional temperature gradients that form over that region (Fig. 4a, 7a), and not entirely to the poleward shifted HC edge.

Another interesting feature highlighted in Figure 9 is that for some variables even the *sign* of the response is different than would otherwise be predicted from the SOM experiments which ignore changes in ocean heat convergence. This applies both to the changes in HC strength (Fig. 9b) and tropospheric column averaged EKE (Fig. 9c) which otherwise decrease in response to increasing CO_2 . This role of the ocean in the behavior of projected changes in northern EKE is consistent with Chemke et al. (2022), who showed that changes in ocean heat convergence are essential for correctly capturing the sign of the projected response in future storm track changes over the North Atlantic.

To further examine the relationship between changes in the HC and changes in the midlatitude eddies, Figure 10 shows the evolution of the responses in the northern HC edge (a), northern HC strength (b), midlatitude EKE (c), and midlatitude baroclinic eddy generation (d). While all fields show a generally similar evolution, the response of the HC edge (Fig. 10a) is more variable and somewhat different compared to the changes in HC strength, midlatitude eddies and midlatitude baroclinicity. This is consistent with the differences in GMST scaling between the HC edge and midlatitude metrics shown in Figure 9.

Finally, while the HC strengthening may be more directly linked to the southward shift of the ITCZ as proposed in previous studies (Zhang and Delworth (2005); Zhang et al. (2010); Orihuela-Pinto et al. (2022)), the similarity of its evolution (Fig. 10b) and scaling with GMST (Fig. 9b) compared with the behavior of the midlatitude eddies (Fig. 10c, Fig. 9c) is striking and suggests that the two may be mechanistically linked. Indeed, previous studies have shown that extratropical wave fluxes impinging on the tropics can strongly influence the HC mass flux (Caballero (2007); Singh et al. (2017)). Though beyond the scope of the current study, future work will focus on better understanding this close correspondence between changes in northern HC strength and midlatitude eddies in the “collapsed” simulations.

c. Energetic Analysis: Bjerknes Compensation in Response to an AMOC Shutdown

The previous section showed that, unlike the global mean thermodynamic response, several measures of NH dynamical sensitivity do not scale linearly with changes in global mean surface temperature. Rather, a collapsed AMOC in our model is accompanied by an abrupt strengthening and northward shift of the HC and northern midlatitude jet. To better understand why these variables exhibit this regime shift we examine the changes in energetics – and their partitioning between the atmosphere and ocean – that arise moving from 2xCO₂ to 3xCO₂ and between the SSP 2-4.5 R and SSP 2-4.5 C members.

1) OCEAN AND ATMOSPHERE COMPENSATION

Figure 11 shows the response in the annual mean northward total (atmosphere + ocean), oceanic and atmospheric transports, relative to the preindustrial control simulation. Between 2xCO₂ and 3xCO₂ and between the SSP 2-4.5 R and SSP 2-4.5 C members there is a large decrease/increase

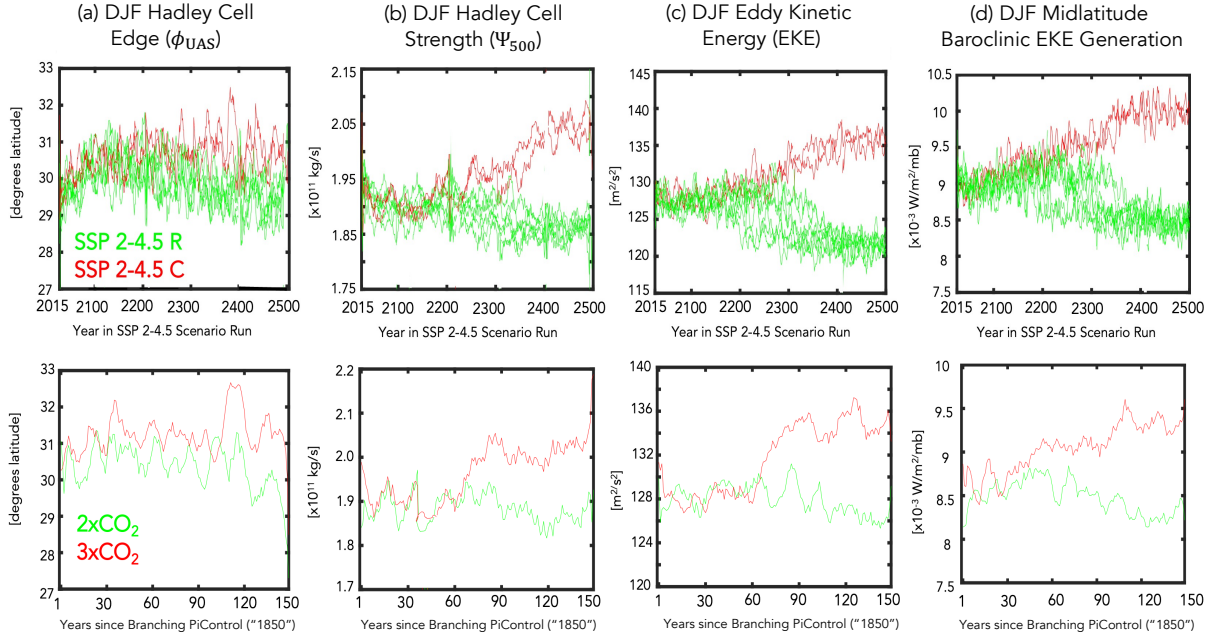


FIG. 10. Evolution of DJF Northern Hemisphere HC edge (a), HC strength (b), midlatitude eddy kinetic energy (c) and midlatitude baroclinic eddy kinetic energy generation (d). The baroclinic eddy generation has been averaged over the same region (300-1000 hPa, 30°N-60°N) as the EKE field, consistent with Figure 9. Comparisons among the SSP 2-4.5 recovered (R) and collapsed (C) ensemble members (top panels) and between the 2xCO₂ and 3xCO₂ runs (bottom panels) are shown in the green and red lines, respectively. A 5-year moving average has been applied to all time series.

in T_O/T_A over northern latitudes with a peak located at $\sim 30-40^\circ\text{N}$. This behavior is reflective of an abrupt Bjerknes compensation that emerges in the model, wherein large anomalies in heat transported by the atmosphere increase to approximately balance large reductions in northward ocean transport (Bjerknes (1964)). More precisely, the reduction in northward ocean heat transport in the SSP 2-4.5 C ensemble members and at 3xCO₂ is approximately 1 PW (Fig. 11), representing a $\sim 50\%$ decrease relative to preindustrial values (Fig. 2b). Magnusdottir and Saravannan (1999) attributed this compensatory response in the atmosphere to high dynamical efficiency of atmospheric eddy transport. Note that the annual mean is shown here to facilitate comparison with the annual mean results presented in previous studies (e.g., Figure 1 in Zhang and Delworth (2005))

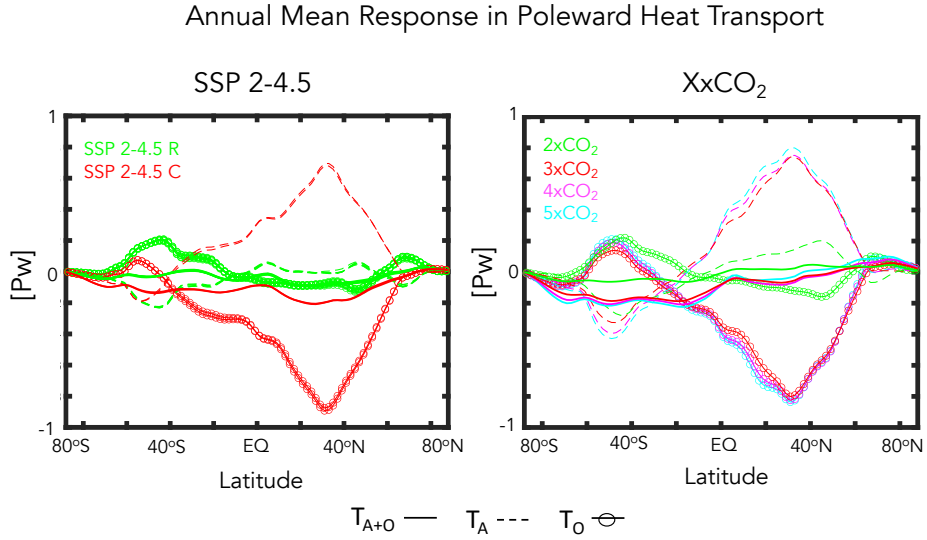


FIG. 11. Changes in the annual mean atmospheric (T_A), oceanic (T_O) and total (atmospheric + oceanic, T_{A+O}) northward energy transport, relative to the preindustrial control simulation. Results from the SSP 2-4.5 ensemble members and the 2-5xCO₂ simulations are shown in the left and right panels. The simulations in which the AMOC collapses (3xCO₂, SSP 2-4.5 C) versus recovers (2xCO₂, SSP 2-4.5 R) are highlighted in the red and green lines, respectively.

and Figure 5 in Zhang et al. (2010)). We note in passing that the responses in the boreal winter transports look very similar (not shown).

What Figure 11 makes clear is that the changes in ocean heat transport are dominated by the changes in the AMOC, as reflected in the magnitude of the compensation occurring at 3xCO₂ (similar to the compensation occurring in the SSP 2-4.5 C ensemble) which saturates, despite further increases in CO₂ (and GMST). This helps to explain the behavior of the dynamical indices discussed in the previous section (Fig. 9), which also saturate at 3xCO₂ and do not increase (rather, decrease) moving to higher CO₂ forcings. A dramatic reduction in poleward ocean heat transport at ~30-40°N was also noted in the CMIP5 historical models in association with strong air-sea interactions within the midlatitude storm tracks (Outten et al. (2018)) and in several future climate integrations performed using the CMIP5 version of the GISS climate model (E2) Rind et al. (2018). In the latter case, however, the near cessation of the AMOC severely limited, but did not entirely shut off, poleward heat transport, which was partly maintained through the ocean

subtropical gyre contribution. Our results also show stronger compensation occurring over SH high latitudes poleward of 40°S.

While the changes in T_O and T_A reflect near entire compensation, this compensation is nonetheless not perfect and slightly negative, resulting in a net reduction in the total northward combined atmospheric and oceanic energy transport. This reduction in net poleward energy transport was also found in Liu et al. (2020), who showed that a weakened AMOC caused a larger energy change at the Earth's surface than at the TOA (their Figure S.5). In particular, over the NAWH region they found that more energy was taken from the atmosphere through surface turbulent heat fluxes, resulting in a situation where the NH atmosphere loses more energy at the surface compared to the energy that is gained at the TOA (through reduced OLR). In the GISS model we also find that there is more energy loss at the surface compared to changes at the TOA and that these are primarily associated with reduced latent heat fluxes (Appendix Figure 4). The reductions in surface latent heat fluxes occur over the North Atlantic and are strongly shaped by changes in evaporation (not shown). The exact extent and nature of this compensation, however, is likely shaped strongly by cloud feedbacks (Zhang et al. (2010)) as discussed more in Section 4b.

2) MOIST VS. DRY ATMOSPHERIC TRANSPORTS

To better understand the nature of the compensation occurring in the GISS model, Figure 12 further decomposes the changes in T_A into changes in the northward transports of latent heat (Fig. 12a) and dry static energy (Fig. 12b). Over the SH the changes in dry and moist static energy nearly compensate in all simulations, resulting in weakly negative northward atmospheric transports poleward of ~40°S in both the XxCO₂ and SSP 2-4.5 runs. Equatorward of ~40°S, however, this behavior transitions in the SSP 2-4.5 C members to net positive northward atmospheric transport from the SH subtropics towards and across the equator (which compensates the reduction in oceanic equatorward heat transport in that region evident in Figure 11). This behavior over the SH subtropics is distinct from what occurs in the XxCO₂ simulations, in which there is overall reduced northward atmospheric transport (and less compensation by the oceanic transports). The fact that the oceanic compensation in this region is weaker at 3xCO₂ (relative to the SSP 2-4.5 C members) may reflect the differences in simulation length between the abrupt CO₂ and SSP 2-4.5 integrations or the fact that at 3xCO₂ there is increased water vapor in the atmosphere in the warmer climate and

Annual Mean Response in Latent Heat, Dry and Moist Static Energy Transport

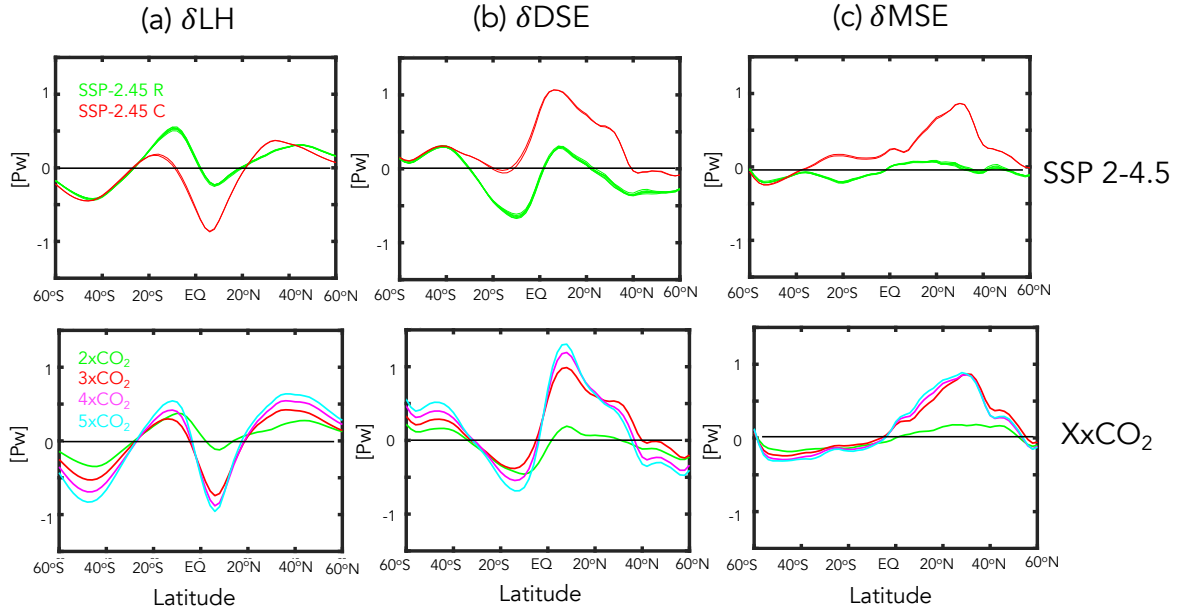


FIG. 12. Changes in the annual mean atmospheric latent heat (a), dry static energy (b) and total moist static energy (c) northward transports, relative to the preindustrial control simulation. Results from the SSP 2-4.5 ensemble members and the 2-5xCO₂ simulations are shown in the top and bottom panels. The simulations in which the AMOC collapses (3xCO₂, SSP 2-4.5 C) versus recovers (2xCO₂, SSP 2-4.5 R) are highlighted in the red and green lines, respectively.

hence increased poleward latent heat transport. Notably, however, the AMOC response in all runs has little effect on extratropical latent heat transport over the Southern Hemisphere extratropics.

Aside from the subtle differences between the 3xCO₂ and SSP 2-4.5 C runs that occur over the SH subtropics, the fact that the changes in dry static energy (DSE) and latent heat transport nearly compensate over southern and tropical latitudes in all runs is consistent with the expectation from Held and Soden (2006). Interestingly, however, this compensation does not occur over northern latitudes spanning ~10°N to ~40°N, resulting in a net increase in poleward moist static energy transport (Fig. 12c). Over these latitudes the increased atmospheric energy transport resulting from an AMOC collapse is almost entirely due to changes in dry static energy, not latent heat transport. In particular, DSE transport exhibits a “jump” between 2xCO₂ and 3xCO₂ (also evident in the differences between the SSP 2-4.5 C and SSP 2-4.5 R members) (Fig. 12b); a similar jump is only evident in the latent heat transports equatorward of 20°N (which, if anything, enhances energy

transport equatorward, not poleward). The jump in DSE transport over the northern extratropics saturates for forcings greater than $3\times\text{CO}_2$. Further analysis of the evolution of the dry static energy transports at different latitudes in the northern hemisphere (not shown) reveals that these changes in DSE transport first emerge around 20°N and propagate thereafter to 40°N .

The fact that the abrupt increase in atmospheric poleward transport derives primarily from changes in DSE transport helps in interpreting why a similar shift emerges in the HC and eddy-driven jet, since the HC fluxes dry static energy poleward (Frierson et al. (2007)). Indeed, previous energetic definitions of the storm track have appealed directly to DSE (e.g. latitude of maximum vertically-integrated dry static energy flux (Hoskins and Valdes (1990))). More recently, Lachmy and Shaw (2018) show that the vertically integrated eddy potential energy flux shifts in same sense as the vertically integrated eddy DSE flux. They then use the Eliassen-Palm flux relation to connect these changes in energy fluxes to changes in the eddy momentum fluxes. Therefore, the fact that these features all shift in concert with each other in our runs should perhaps not be too surprising.

4. Discussion

a. Caveats Concerning Model Biases

One important caveat with our results relates to known biases in vertical mixing in the ocean component of the GISS model, as discussed in Miller et al. (2021). This biased mixing is likely related to why E2.1 exhibits a more sensitive AMOC response to a quadrupling of CO_2 , compared to some other CMIP6 models (KB2021). In addition, Rind et al. (2020) showed that the parameterization of rainfall evaporation associated with moist convective precipitation has a strong influence on the AMOC sensitivity to greenhouse gas forcing in the E2.1 (and higher top E2.2) models, likely via its effect on moisture loading in the atmosphere. Thus, in addition to oceanic processes, atmospheric parameterizations could also be influencing this result.

Along with biases in vertical mixing, the ocean component of E2.1 is also low resolution (one degree). This likely has direct implications for the stability of the AMOC, as discussed in AR2023 (see references therein). In particular, the stability of the AMOC will differ between low resolution climate models, which exhibit a negative salt-advection feedback (leading to salinification of the subpolar gyre and AMOC recovery), and eddy-permitting models, which tend to exhibit a stable AMOC-off state. We emphasize here, however, that throughout we have focused on the response of

the atmospheric circulation given a collapse in the AMOC. Thus, while the particular mechanisms by which the AMOC is weakened (and subsequently recovers) in E2.1 may be model-specific, our focus has been on quantifying the atmospheric changes. We also note that Mitevski et al. (2021) showed that the behavior of the AMOC in E2.1 was similar to the response in CESM-LE; furthermore that model also featured a nonlinear response in GMST related to a collapse of the AMOC, albeit one occurring at the transition between 3xCO₂ and 4xCO₂.

b. Bjerknes Compensation: Cloud Feedbacks and Dry Versus Moist Energy Transports

A key result from our study is that a collapse of the AMOC results in a regime shift in various components of the NH large-scale circulation and this shift is reflective of an abrupt Bjerknes compensation that emerges at 3xCO₂ and in the SSP 2-4.5 C ensemble members. There are several aspects of this compensation, however, that require closer examination. Among others, these include:

1) INFLUENCE OF CLOUD FEEDBACKS

Mitevski et al. (2022) showed that nonlinearity in ECS occurring between 2xCO₂ and 3xCO₂ in our model was related to nonlinear variations in the atmospheric feedback parameter and not to changes in radiative forcing. At the same time, the strength of the Bjerknes compensation in our model will likely depend on cloud feedbacks, as the right-hand-side of Equation (1) makes clear (via the F_T and F_S terms). For example, Zhang et al. (2010) showed a strong sensitivity of the tropical climates' response to a freshwater hosing forcing to changes in cloud feedbacks, showing that in a model with no cloud feedbacks the tropical response to the weakening of the AMOC (including its southward ITCZ shift) was much smaller. Thus, while the overall Bjerknes compensation occurring in our model is generally consistent (in its meridional distribution and amplitude) with the results from other similar studies, the exact details of how compensation occurs is likely to be sensitive to local climate feedbacks which may be model-dependent and/or poorly constrained by observations. Future work will focus on better understanding how changes in cloud feedbacks modulate the response of the atmosphere to a weakened AMOC in our model.

2) ATMOSPHERIC DRY VS. MOIST COMPENSATION

One interesting result from this study is that the large compensation in poleward atmospheric transport that occurs as the AMOC collapses is primarily related to increases in the northward transport of dry static energy poleward of 20°N (coincident with the edge of the non-monotonically shifting HC edge) (Fig. 12). This result is initially surprising as it downplays the compensation that occurs through changes in latent heat transport over northern midlatitudes. Thus, while our results do show a compensatory latent heat transport occurring in the tropics, this does not occur over the NH extratropics and is therefore not fundamentally associated with the non-monotonic behavior in the NH HC edge and midlatitude eddy-driven jet.

The diminished importance of the latent heat transports over northern midlatitudes is initially surprising, given that warming in response to increased CO₂ results in an overall increase in atmospheric water vapor. Upon further reflection, however, this effect of enhanced global warming needs to be considered in the context of both the reduced Arctic warming and poleward shifted EKE evident in Figure 4. The former can, via cooling, reduce the total moisture available for northward transport, while the latter would impact the efficiency with which subtropical moisture is transported poleward to higher latitudes. In our results it appears that these changes compensate, resulting in no net AMOC imprint on the latent heat transports over northern extratropical latitudes (Fig. 12a, top). While disentangling these contributions is beyond the scope of this study, we do comment on the consistent results shown in Figure S5 of Mitevski et al. (2021), who identified a much stronger non-monotonicity present in the edge of the dry zone (P-E) compared to NH specific humidity. While this suggests that the circulation changes are themselves responsible for the behavior of the latent heat transports (and not vice versa), more work is needed to understand the underlying mechanism present in our model and whether this behavior is also exhibited in other models (or the real atmosphere).

5. Conclusions

Here we have documented the atmospheric response to a CO₂-induced AMOC collapse using the CMIP6 version of the NASA GISS climate model (E2.1). Using simulations from an identically forced (SSP 2-4.5) ensemble in which the AMOC collapses and recovers in two and eight members, respectively, we have isolated the atmospheric response to a spontaneous collapse

of the AMOC in the context of a warming climate, absent any external perturbations that may interfere with the model’s internal dynamics. By comparison, previous studies have all needed to employ (negative) freshwater flux perturbations or similar AMOC “locking” methods (Liu et al. (2020), Orihuela-Pinto et al. (2022)). We then placed the atmospheric response in the SSP 2-4.5 simulations in the broader context of a set of integrations in which CO₂ is abruptly increased, run both using fully coupled atmosphere-ocean (FOM) and slab-ocean (SOM) configurations, in which changes in ocean heat flux convergences are respectively included and neglected.

Our main results are as follows:

- In our model a sustained decline and eventual collapse of the AMOC results in a strengthening of the NH HC and the northern midlatitude jet, as well as an abrupt northward shift of the HC edge in the lower troposphere. Quite remarkably, these features dominate the large-scale atmospheric circulation response that occurs in the NH moving from 2xCO₂ to 3xCO₂.
- For certain variables (i.e., HC strength, EKE) an ultimate collapse of the AMOC produces changes that are *opposite* in sign to the response to increased CO₂ forcing occurring in the absence of ocean circulation changes.
- The regime shift in the NH large-scale circulation reflects an abrupt Bjerknes compensation that emerges in the 3xCO₂ and collapsed SSP 2-4.5 C simulations. This compensation is located further south (~40°N) of what is often considered to be the main region of maximum ocean-atmosphere compensation (70°N) (Shaffrey and Sutton (2006)) and reflects a key role for the midlatitude storm tracks in the coupled system’s response to a warmer climate.
- The impact of the AMOC on the large-scale NH circulation occurs mainly through its influence on mean free-tropospheric temperature gradients, not GMST. This finding reinforces growing evidence that the climate’s “dynamical sensitivity” does not scale with equilibrium climate sensitivity (Grise and Polvani (2016), Ceppi et al. (2018)), particularly in the presence of a collapsed AMOC .

The regime shift in NH dynamics resulting from an AMOC collapse in our model is, to the best of our knowledge, the first time that such behavior has been documented for a CMIP class model. While previous studies have also reported nonlinear behaviors in HC strength (Levine and

915 Schneider (2011), O'Reilly et al. (2016)) these studies have employed mainly idealized models. In
916 addition to the changes in the HC we also identify a regime shift in the behavior of the northern storm
917 tracks. This result brings to mind the findings from Caballero and Langen (2005), who showed that
918 poleward energy transport increases over a range of increasing surface temperature but saturates
919 in the low-gradient, high temperature regime. As in our study, they attribute this “low-gradient
920 paradox” to increasing tropospheric static stability and the poleward migration of the storm tracks.
921 However, they too employed a highly idealized (aquaplanet) model and find that this saturation in
922 storm track behavior is related to a saturation of latent heat transport. Our results, by comparison,
923 highlight the role of compensatory dry static energy transports and suggests that studies accounting
924 for dynamic ocean-atmospheric coupling (i.e., changes in vertical and horizontal ocean heat fluxes)
925 may come to different conclusions about the nature of compensation in the atmosphere.

926 In addition to contributing to improved understanding of the coupled atmosphere-ocean response
927 to a weakening of the AMOC, our results also have a practical implication for the purpose of
928 developing storylines of atmospheric circulation changes (Zappa and Shepherd (2017)) and for
929 interpreting model differences in projected storm tracks. In particular, while the use of “global
930 warming levels” applied throughout the IPCC AR6 report may suffice for understanding the global
931 hydrological cycle (Hausfather et al. (2022)) here we have shown that this does not hold true for
932 projections of the NH jet stream and HC edge. This underscores the need to understand the direct
933 impact of the AMOC on meridional temperature gradients and not only on surface temperature.

934 Finally, preliminary analysis of the high-top GISS climate model (E2.2 (Rind et al. (2020), Orbe
935 et al. (2020)) suggests a different sensitivity of the AMOC compared to E2.1 (occurring between
936 $3\times\text{CO}_2$ and $4\times\text{CO}_2$). Understanding these differences and how they are reflected in different
937 Bjerknes compensations will be described in a follow-up paper.

938 *Acknowledgments.* C.O. thanks Ivan Mitevski for processing the zonally varying eddy kinetic
939 energy fields that were used as part of this analysis. Climate modeling at GISS is supported
940 by the NASA Modeling, Analysis and Prediction program, and resources supporting this work
941 were provided by the NASA High-End Computing (HEC) Program through the NASA Center for
942 Climate Simulation (NCCS) at Goddard Space Flight Center.

943 *Data availability statement.* The CMIP6 SSP 2-4.5 data used in this study is available from
944 the Earth System Grid Federation (ESGF) (<https://esgf-node.llnl.gov/search/cmip6/>)
945 or from the NASA Center for Climate Simulations (NCCS) (<https://portal.nccs.nasa.gov/datashare/giss/cmip6/>). The specific simulations used here are a subset of the historical
946 r[1-10]i1p1f2 (doi:10.22033/ESGF/CMIP6.7127) and SSP 2-4.5 r[1-10]i1p1f2 (doi:10.
947 22033/ESGF/CMIP6.7415) runs. The XxCO₂ data used to produce the figures in the study is
948 publicly available in a Zenodo repository at <https://doi.org/10.5281/zenodo.3901624>.
949 The authors acknowledge the World Climate Research Programme's Working Group on Coupled
950 Modeling and we thank all climate modeling groups for making available their model output.
951 All GISS ModelE components are open source and available at [https://www.giss.nasa.gov/](https://www.giss.nasa.gov/tools/modelE/)
952 [tools/modelE/](https://www.giss.nasa.gov/tools/modelE/).
953

Appendix Figures

Evolution of DJF Response in Sea Surface Temperature (δ SST)

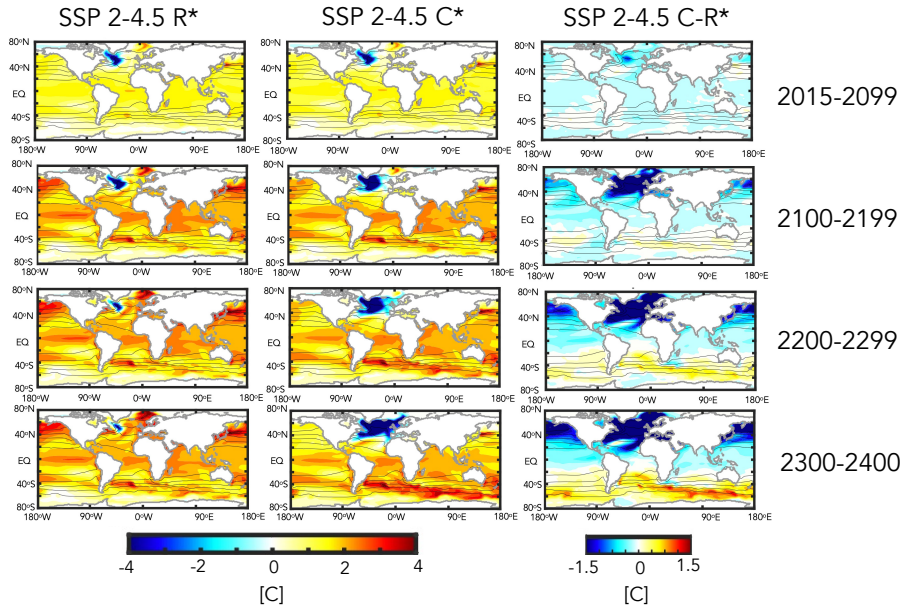


FIG. A1. The evolution of the DJF sea surface temperature difference, relative to the preindustrial control simulation, in one of the SSP 2-4.5 recovered (R) (left) and collapsed (C) ensemble members (middle). The difference between the SSP 2-4.5 recovered and collapsed ensemble members is also shown (right). Note that only one ensemble member is used due to the different recovery times of the AMOC among the “recovered” ensemble members prior to year 2400. Climatological mean values from the preindustrial control simulation are denoted in the black contours.

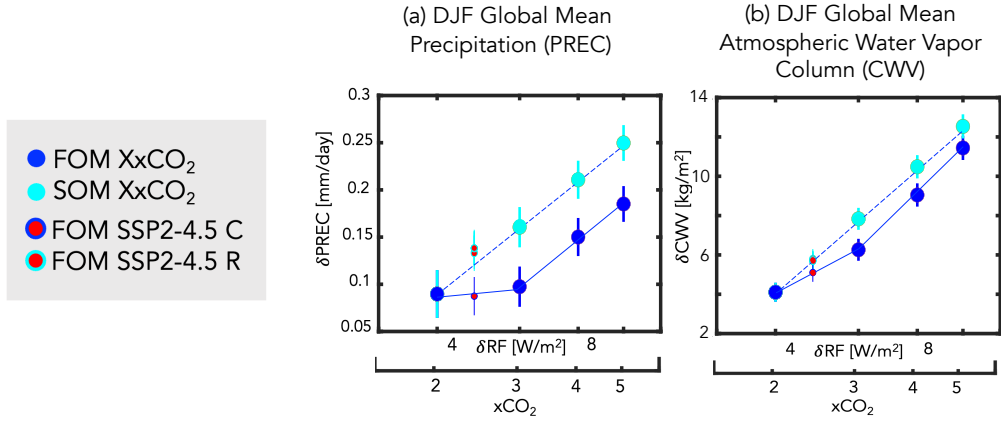


FIG. A2. Changes in DJF global mean precipitation (a) and atmospheric column water vapor (b), plotted as a function of the associated radiative forcing (RF), calculated from the expression $5.35 \ln(Nx\text{CO}_2/1x\text{CO}_2)$ (Byrne and Goldblatt (2014)) where, for each run, N is the CO_2 multiple of the PI value (2.4, for the case of the SSP 2-4.5 ensemble members). Results from the abrupt 2-5 $x\text{CO}_2$ fully coupled atmosphere-ocean model (FOM) and slab ocean model (SOM) results are shown in the blue and cyan filled circles. The FOM SSP 2-4.5 recovered and collapsed ensemble members are also shown in the red circles (cyan and blue outlines, respectively). Interannual variability for each metric is indicated by the vertical bars.

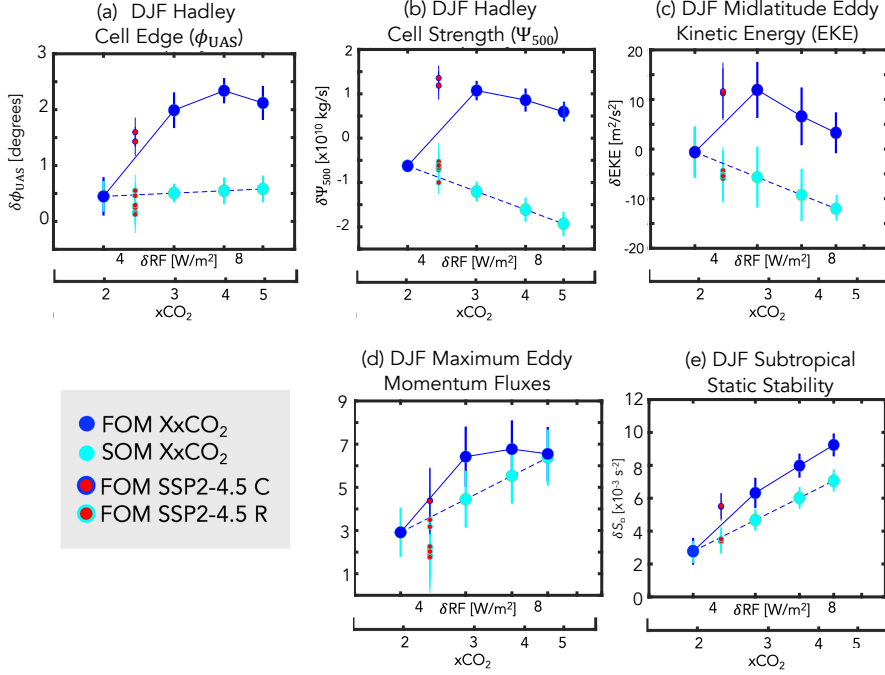
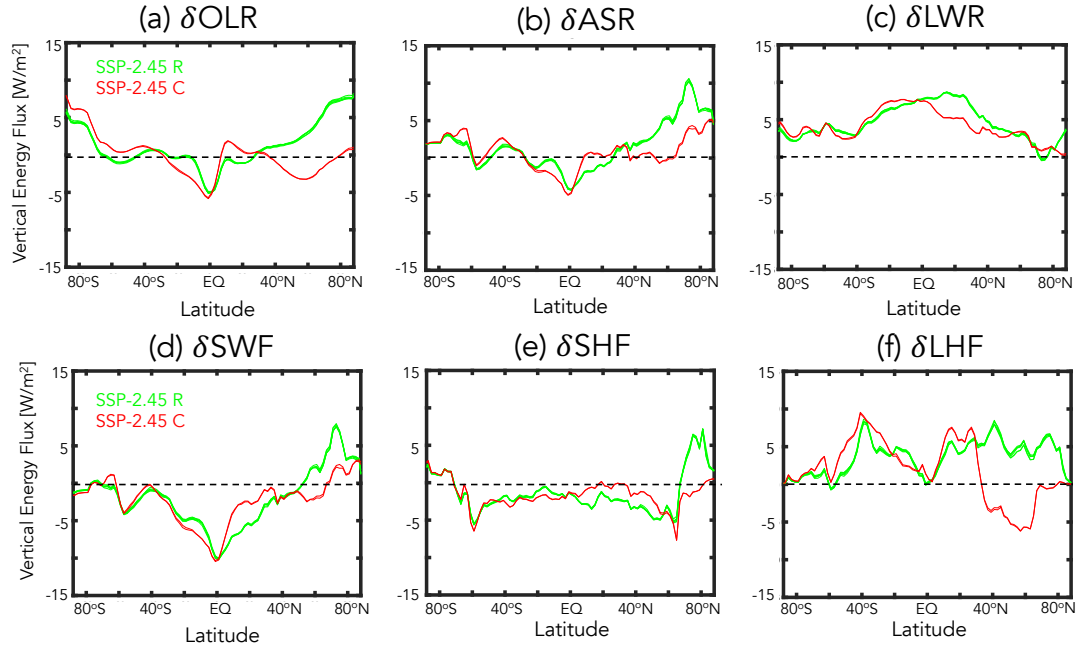


FIG. A3. Changes in various DJF Northern Hemisphere (NH) dynamical metrics, plotted as a function of associated radiative forcing. Specifically, shown are the HC edge (ϕ_{UAS}) (a), HC strength (Ψ_{500}) (b), NH column eddy kinetic energy (EKE) (c), latitude of the maximum NH eddy momentum fluxes (d) and NH subtropical dry static stability (e). The quantities in (a), (b) and (d) are defined in Section 2, while the zonally averaged EKE and static stability changes have both been averaged over 300-1000 hPa and over 30°N-60°N and 20°N-40°N, respectively. Results from the abrupt 2-5 xCO_2 fully coupled atmosphere-ocean model (FOM) and slab ocean model (SOM) results are shown in the blue and cyan filled circles. The FOM SSP 2-4.5 recovered and collapsed ensemble members are shown in the red circles (cyan and blue outlines, respectively). Interannual variability for each metric is indicated by the vertical bars.



978 FIG. A4. Changes in the annual mean top of the atmosphere outgoing longwave radiation (OLR) (a) and
 979 absorbed shortwave radiation (ASR) (b) and the downward fluxes of radiation at the surface, decomposed into
 980 longwave (LWF) (c) and shortwave (SWF) (d) components. The fluxes of latent and sensible heat at the surface
 981 (LHF and SHF) are shown in (e) and (f), respectively. All changes are shown for the SSP 2-4.5 collapsed (C)
 982 (red) and SSP 2-4.5 recovered (R) (green) ensemble members and are defined relative to the preindustrial control
 983 simulation.

References

- Adam, O., and Coauthors, 2018: The TropD software package (v1): Standardized methods for calculating tropical-width diagnostics. *Geoscientific Model Development*, **11** (10), 4339–4357.
- Bellomo, K., M. Angeloni, S. Corti, and J. von Hardenberg, 2021: Future climate change shaped by inter-model differences in Atlantic meridional overturning circulation response. *Nature Communications*, **12** (1), 1–10.
- Bjerknes, J., 1964: Atlantic air-sea interaction. *Advances in geophysics*, Vol. 10, Elsevier, 1–82.
- Brayshaw, D. J., T. Woollings, and M. Vellinga, 2009: Tropical and extratropical responses of the North Atlantic atmospheric circulation to a sustained weakening of the MOC. *Journal of Climate*, **22** (11), 3146–3155.
- Byrne, B., and C. Goldblatt, 2014: Radiative forcing at high concentrations of well-mixed greenhouse gases. *Geophysical Research Letters*, **41** (1), 152–160.
- Caballero, R., 2007: Role of eddies in the interannual variability of Hadley cell strength. *Geophysical Research Letters*, **34** (22).
- Caballero, R., and P. L. Langen, 2005: The dynamic range of poleward energy transport in an atmospheric general circulation model. *Geophysical Research Letters*, **32** (2).
- Caesar, L., S. Rahmstorf, A. Robinson, G. Feulner, and V. Saba, 2018: Observed fingerprint of a weakening Atlantic ocean overturning circulation. *Nature*, **556** (7700), 191–196.
- Ceppi, P., G. Zappa, T. G. Shepherd, and J. M. Gregory, 2018: Fast and slow components of the extratropical atmospheric circulation response to CO₂ forcing. *Journal of Climate*, **31** (3), 1091–1105.
- Chemke, R., and L. M. Polvani, 2019: Exploiting the abrupt 4×CO₂ scenario to elucidate tropical expansion mechanisms. *Journal of Climate*, **32** (3), 859–875.
- Chemke, R., L. Zanna, C. Orbe, L. T. Sentman, and L. M. Polvani, 2022: The future intensification of the North Atlantic winter storm track: the key role of dynamic ocean coupling. *Journal of Climate*, **35** (8), 2407–2421.

- 1010 Cheng, W., J. C. Chiang, and D. Zhang, 2013: Atlantic meridional overturning circulation (AMOC)
1011 in CMIP5 models: RCP and historical simulations. *Journal of Climate*, **26 (18)**, 7187–7197.
- 1012 Deser, C., and A. S. Phillips, 2009: Atmospheric circulation trends, 1950–2000: The relative roles
1013 of sea surface temperature forcing and direct atmospheric radiative forcing. *Journal of Climate*,
1014 **22 (2)**, 396–413.
- 1015 Drijfhout, S., G. J. Van Oldenborgh, and A. Cimadoribus, 2012: Is a decline of AMOC causing the
1016 warming hole above the North Atlantic in observed and modeled warming patterns? *Journal of*
1017 *Climate*, **25 (24)**, 8373–8379.
- 1018 Frierson, D. M., I. M. Held, and P. Zurita-Gotor, 2007: A gray-radiation aquaplanet moist GCM.
1019 Part II: Energy transports in altered climates. *Journal of the Atmospheric Sciences*, **64 (5)**,
1020 1680–1693.
- 1021 Gervais, M., J. Shaman, and Y. Kushnir, 2019: Impacts of the North Atlantic warming hole in
1022 future climate projections: Mean atmospheric circulation and the North Atlantic jet. *Journal of*
1023 *Climate*, **32 (10)**, 2673–2689.
- 1024 Grise, K. M., and L. M. Polvani, 2014: The response of midlatitude jets to increased CO₂:
1025 Distinguishing the roles of sea surface temperature and direct radiative forcing. *Geophysical*
1026 *Research Letters*, **41 (19)**, 6863–6871.
- 1027 Grise, K. M., and L. M. Polvani, 2016: Is climate sensitivity related to dynamical sensitivity?
1028 *Journal of Geophysical Research: Atmospheres*, **121 (10)**, 5159–5176.
- 1029 Grise, K. M., and L. M. Polvani, 2017: Understanding the time scales of the tropospheric circulation
1030 response to abrupt CO₂ forcing in the southern hemisphere: Seasonality and the role of the
1031 stratosphere. *Journal of Climate*, **30 (21)**, 8497–8515.
- 1032 Haarsma, R., F. Selten, and S. Drijfhout, 2015: Decelerating Atlantic meridional overturning
1033 circulation main cause of future west european summer circulation changes. *Environmental*
1034 *Research Letters*, **10 (9)**.
- 1035 Hausfather, Z., K. Marvel, G. A. Schmidt, J. W. Nielsen-Gammon, and M. Zelinka, 2022: Climate
1036 simulations: Recognize the ‘hot model’ problem. Nature Publishing Group.

- 1037 Held, I. M., and B. J. Soden, 2006: Robust responses of the hydrological cycle to global warming.
1038 *Journal of Climate*, **19** (21), 5686–5699.
- 1039 Hoskins, B. J., and P. J. Valdes, 1990: On the existence of storm-tracks. *Journal of Atmospheric*
1040 *Sciences*, **47** (15), 1854–1864.
- 1041 Jackson, L., R. Kahana, T. Graham, M. Ringer, T. Woollings, J. Mecking, and R. Wood, 2015:
1042 Global and European climate impacts of a slowdown of the AMOC in a high resolution GCM.
1043 *Climate Dynamics*, **45** (11), 3299–3316.
- 1044 James, R., R. Washington, C.-F. Schleussner, J. Rogelj, and D. Conway, 2017: Characterizing half-
1045 a-degree difference: a review of methods for identifying regional climate responses to global
1046 warming targets. *Wiley Interdisciplinary Reviews: Climate Change*, **8** (2), e457.
- 1047 Josey, S. A., J. J.-M. Hirschi, B. Sinha, A. Ducheze, J. P. Grist, and R. Marsh, 2018: The recent
1048 Atlantic cold anomaly: Causes, consequences, and related phenomena. *Annual Review of Marine*
1049 *Science*, **10**, 475–501.
- 1050 Kelley, M., and Coauthors, 2020: GISS-E2.1: Configurations and climatology. *Journal of Advances*
1051 *in Modeling Earth Systems*, **12** (8), e2019MS002 025.
- 1052 Lachmy, O., and T. Shaw, 2018: Connecting the energy and momentum flux response to climate
1053 change using the Eliassen-Palm relation. *Journal of Climate*, **31** (18), 7401–7416.
- 1054 Lau, N.-C., H. Tennekes, and J. M. Wallace, 1978: Maintenance of the momentum flux by transient
1055 eddies in the upper troposphere. *Journal of Atmospheric Sciences*, **35** (1), 139–147.
- 1056 Levine, X. J., and T. Schneider, 2011: Response of the Hadley circulation to climate change in
1057 an aquaplanet GCM coupled to a simple representation of ocean heat transport. *Journal of the*
1058 *Atmospheric Sciences*, **68** (4), 769–783.
- 1059 Lim, G. H., and J. M. Wallace, 1991: Structure and evolution of baroclinic waves as inferred from
1060 regression analysis. *Journal of Atmospheric Sciences*, **48** (15), 1718–1732.
- 1061 Liu, W., A. V. Fedorov, S.-P. Xie, and S. Hu, 2020: Climate impacts of a weakened Atlantic
1062 Meridional Overturning Circulation in a warming climate. *Science Advances*, **6** (26), eaaz4876.

- 1063 Lorenz, E. N., 1955: Available potential energy and the maintenance of the general circulation.
1064 *Tellus*, **7** (2), 157–167.
- 1065 Magnusdottir, G., and R. Saravannan, 1999: The response of atmospheric heat transport to zonally-
1066 averaged SST trends. *Tellus A: Dynamic Meteorology and Oceanography*, **51** (5), 815–832.
- 1067 Marshall, J., J. R. Scott, K. C. Armour, J.-M. Campin, M. Kelley, and A. Romanou, 2015: The
1068 ocean’s role in the transient response of climate to abrupt greenhouse gas forcing. *Climate*
1069 *Dynamics*, **44** (7), 2287–2299.
- 1070 Meinshausen, M., and Coauthors, 2020: The shared socio-economic pathway (SSP) greenhouse
1071 gas concentrations and their extensions to 2500. *Geoscientific Model Development*, **13** (8),
1072 3571–3605.
- 1073 Menary, M. B., and R. A. Wood, 2018: An anatomy of the projected North Atlantic warming hole
1074 in CMIP5 models. *Climate Dynamics*, **50** (7), 3063–3080.
- 1075 Menzel, M. E., D. Waugh, and K. Grise, 2019: Disconnect between Hadley cell and subtropical jet
1076 variability and response to increased CO₂. *Geophysical Research Letters*, **46** (12), 7045–7053.
- 1077 Miller, R. L., and Coauthors, 2021: CMIP6 historical simulations (1850–2014) with GISS-E2. 1.
1078 *Journal of Advances in Modeling Earth Systems*, **13** (1), e2019MS002 034.
- 1079 Mitevski, I., C. Orbe, R. Chemke, L. Nazarenko, and L. M. Polvani, 2021: Non-monotonic
1080 response of the climate system to abrupt CO₂ forcing. *Geophysical Research Letters*, **48** (6),
1081 e2020GL090 861.
- 1082 Mitevski, I., L. M. Polvani, and C. Orbe, 2022: Asymmetric warming/cooling response to CO₂
1083 increase/decrease mainly due to non-logarithmic forcing, not feedbacks. *Geophysical Research*
1084 *Letters*, **49** (5), e2021GL097 133.
- 1085 Nazarenko, L. S., and Coauthors, 2022: Future climate change under SSP emission scenarios with
1086 GISS-E2. 1. *Journal of Advances in Modeling Earth Systems*, e2021MS002871.
- 1087 Orbe, C., and Coauthors, 2020: GISS model E2. 2: A climate model optimized for the middle
1088 atmosphere—2. Validation of large-scale transport and evaluation of climate response. *Journal*
1089 *of Geophysical Research: Atmospheres*, **125** (24), e2020JD033 151.

- 1090 O'Reilly, C. H., M. Huber, T. Woollings, and L. Zanna, 2016: The signature of low-frequency
1091 oceanic forcing in the Atlantic Multidecadal Oscillation. *Geophysical Research Letters*, **43** (6),
1092 2810–2818.
- 1093 Orihuela-Pinto, B., M. H. England, and A. S. Taschetto, 2022: Interbasin and interhemispheric
1094 impacts of a collapsed Atlantic Overturning Circulation. *Nature Climate Change*, 1–8.
- 1095 Outten, S., I. Esau, and O. H. Otterå, 2018: Bjerknes compensation in the CMIP5 climate models.
1096 *Journal of Climate*, **31** (21), 8745–8760.
- 1097 Pedro, J. B., M. Jochum, C. Buizert, F. He, S. Barker, and S. O. Rasmussen, 2018: Beyond
1098 the bipolar seesaw: Toward a process understanding of interhemispheric coupling. *Quaternary*
1099 *Science Reviews*, **192**, 27–46.
- 1100 Rahmstorf, S., J. E. Box, G. Feulner, M. E. Mann, A. Robinson, S. Rutherford, and E. J. Schaffer-
1101 nicht, 2015: Exceptional twentieth-century slowdown in Atlantic Ocean overturning circulation.
1102 *Nature Climate Change*, **5** (5), 475–480.
- 1103 Riahi, K., and Coauthors, 2011: RCP 8.5—A scenario of comparatively high greenhouse gas
1104 emissions. *Climatic Change*, **109**, 33–57.
- 1105 Rind, D., G. A. Schmidt, J. Jonas, R. Miller, L. Nazarenko, M. Kelley, and J. Romanski, 2018:
1106 Multicentury instability of the Atlantic meridional circulation in rapid warming simulations with
1107 GISS ModelE2. *Journal of Geophysical Research: Atmospheres*, **123** (12), 6331–6355.
- 1108 Rind, D., and Coauthors, 2020: GISS Model E2. 2: A climate model optimized for the mid-
1109 dle atmosphere—Model structure, climatology, variability, and climate sensitivity. *Journal of*
1110 *Geophysical Research: Atmospheres*, **125** (10), e2019JD032 204.
- 1111 Robson, J., P. Ortega, and R. Sutton, 2016: A reversal of climatic trends in the North Atlantic since
1112 2005. *Nature Geoscience*, **9** (7), 513–517.
- 1113 Romanou, A., and Coauthors, 2023: Stochastic bifurcation of the north atlantic circulation under
1114 a mid-range future climate scenario with the nasa-giss modele. *Journal of Climate*, 1–49.
- 1115 Santer, B. D., T. M. Wigley, M. E. Schlesinger, and J. F. Mitchell, 1990: Developing climate
1116 scenarios from equilibrium GCM results.

1117 Schmidt, D. F., and K. M. Grise, 2017: The response of local precipitation and sea level pressure
1118 to Hadley cell expansion. *Geophysical Research Letters*, **44** (20), 10–573.

1119 Schneider, T., 2006: The general circulation of the atmosphere. *Annu. Rev. Earth Planet. Sci.*, **34**,
1120 655–688.

1121 Shaffrey, L., and R. Sutton, 2006: Bjerknes compensation and the decadal variability of the energy
1122 transports in a coupled climate model. *Journal of Climate*, **19** (7), 1167–1181.

1123 Shaw, T., and A. Voigt, 2015: Tug of war on summertime circulation between radiative forcing
1124 and sea surface warming. *Nature Geoscience*, **8** (7), 560–566.

1125 Shepherd, T. G., 2014: Atmospheric circulation as a source of uncertainty in climate change
1126 projections. *Nature Geoscience*, **7** (10), 703–708.

1127 Singh, M. S., Z. Kuang, and Y. Tian, 2017: Eddy influences on the strength of the hadley
1128 circulation: Dynamic and thermodynamic perspectives. *Journal of the Atmospheric Sciences*,
1129 **74** (2), 467–486.

1130 Smith, D. M., R. Eade, N. J. Dunstone, D. Fereday, J. M. Murphy, H. Pohlmann, and A. A. Scaife,
1131 2010: Skilful multi-year predictions of Atlantic hurricane frequency. *Nature Geoscience*, **3** (12),
1132 846–849.

1133 Tebaldi, C., and J. M. Arblaster, 2014: Pattern scaling: Its strengths and limitations, and an update
1134 on the latest model simulations. *Climatic Change*, **122** (3), 459–471.

1135 Timmermann, A., and Coauthors, 2007: The influence of a weakening of the Atlantic meridional
1136 overturning circulation on ENSO. *Journal of Climate*, **20** (19), 4899–4919.

1137 Vellinga, M., and R. A. Wood, 2008: Impacts of thermohaline circulation shutdown in the twenty-
1138 first century. *Climatic Change*, **91** (1), 43–63.

1139 Vial, J., C. Cassou, F. Codron, S. Bony, and Y. Ruprich-Robert, 2018: Influence of the Atlantic
1140 meridional overturning circulation on the tropical climate response to CO₂ forcing. *Geophysical
1141 Research Letters*, **45** (16), 8519–8528.

1142 Waugh, D. W., and Coauthors, 2018: Revisiting the relationship among metrics of tropical expan-
1143 sion. *Journal of Climate*, **31** (18), 7565–7581.

- 1144 Weijer, W., W. Cheng, O. A. Garuba, A. Hu, and B. Nadiga, 2020: CMIP6 models predict
1145 significant 21st century decline of the Atlantic meridional overturning circulation. *Geophysical*
1146 *Research Letters*, **47** (12), e2019GL086075.
- 1147 Woollings, T., J. M. Gregory, J. G. Pinto, M. Reyers, and D. J. Brayshaw, 2012: Response of
1148 the North Atlantic storm track to climate change shaped by ocean–atmosphere coupling. *Nature*
1149 *Geoscience*, **5** (5), 313–317.
- 1150 Wu, L., C. Li, C. Yang, and S.-P. Xie, 2008: Global teleconnections in response to a shutdown of
1151 the Atlantic meridional overturning circulation. *Journal of Climate*, **21** (12), 3002–3019.
- 1152 Zappa, G., and T. G. Shepherd, 2017: Storylines of atmospheric circulation change for european
1153 regional climate impact assessment. *Journal of Climate*, **30** (16), 6561–6577.
- 1154 Zhang, R., and T. L. Delworth, 2005: Simulated tropical response to a substantial weakening of
1155 the Atlantic thermohaline circulation. *Journal of Climate*, **18** (12), 1853–1860.
- 1156 Zhang, R., and T. L. Delworth, 2006: Impact of Atlantic multidecadal oscillations on India/Sahel
1157 rainfall and Atlantic hurricanes. *Geophysical Research Letters*, **33** (17).
- 1158 Zhang, R., S. M. Kang, and I. M. Held, 2010: Sensitivity of climate change induced by the
1159 weakening of the Atlantic meridional overturning circulation to cloud feedback. *Journal of*
1160 *Climate*, **23** (2), 378–389.